Low order multipole maps of CMB anisotropy derived from WMAP

P. Bielewicz,^{1,2} * K.M. Górski^{2,3} and A.J. Banday⁴

- ¹ Institute of Theoretical Physics, Warsaw University, ul. Hoża 69, PL-00-681 Warsaw
- ² Warsaw University Observatory, Aleje Ujazdowskie 4, 00-478 Warszawa, Poland
- ³ JPL, M/S 169/327, 4800 Oak Grove Drive, Pasadena CA 91109
- ⁴ Max-Planck-Institut fuer Astrophysik, Karl-Schwarzschild-Str. 1, Postfach 1317, D-85741 Garching bei Muenchen, Germany

ABSTRACT

Recent analyses of the WMAP data have suggested that the low order multipoles of the CMB anisotropy distribution show cosmologically interesting and unexpected morphologies and amplitudes. In this paper, we apply a power equalization (PE) filter to the high latitude *WMAP* data in order to reconstruct these low- ℓ multipoles free from the largest Galactic foreground modelling uncertainties in the Galactic plane. The characteristic spatial distributions of the modes of order $\ell = 2, 3, 4, 5$ have been determined as a function of frequency, sky coverage and two methods for foreground correction – using the template fitting results of Bennett et al. (2003b) and by a simple linear projection scheme assuming the spectral dependence of the foreground components. Although the derived multipole maps are statistically consistent with previous estimates from Tegmark et al. (2003) and Efstathiou (2003a), our analyses suggest that the K and Ka frequency bands remain significantly contaminated by residual foreground emission for the WMAP Kp2 mask. However, the $\ell = 3, 4, 5$ multipole maps for the Q, V and W channels indicate that, after foreground cleaning, these multipoles are dominated by the CMB anisotropy component. We confirm the Tegmark et al. (2003) result that the octopole does indeed show structure in which its hot and cold spots are centred on a single plane in the sky, and show further that this is very stable with respect to the applied mask and foreground correction. The estimated quadrupole is much less stable showing nonnegligible dependence on the Galactic foreground correction. Including these uncertainties is likely to weaken the statistical significance of the claimed alignment between the quadrupole and octopole. Nevertheless, these anisotropy patterns are also present for in COBE-DMR data, and are unlikely to be associated with instrumental systematic artifacts.

Key words: cosmic microwave background–cosmology: observations

1 INTRODUCTION

In the standard cosmological interpretation, the distribution and statistical properties of the Cosmic Microwave Background (CMB) temperature anisotropies reflect the properties of the universe approximately 300 000 years after the Big Bang. The simplest inflationary models of the origin of the primordial density fluctuations predict statistically isotropic and Gaussian fluctuations for the CMB. Thus in the conventional approach, where the temperature anisotropy field, $\Delta T(\theta,\phi)$, is expanded as a sum over the spherical harmonic basis on the sphere

$$\Delta T(\theta, \phi) = \sum_{\ell=1}^{\infty} \sum_{m=-\ell}^{\ell} a_{\ell m} Y_{\ell m}(\theta, \phi)$$
 (1)

the decomposition coefficients, $a_{\ell m}$, are independent, Gaussian distributed stochastic variables. Then, due to statistical isotropy, their

variances $C_{\ell} = \langle |a_{\ell m}|^2 \rangle$ depend only on ℓ . The validity of these predictions can be constrained by direct observation of the CMB anisotropy.

The sum over m for a given ℓ , $\Delta T_{\ell}(\theta,\phi)$, is then a multipole map of order ℓ , and typically represents the CMB fluctuations on angular scale $\sim 1/\ell$. The lowest multipoles of the CMB anisotropy, in particular the dipole ($\ell=1$), quadrupole ($\ell=2$) and octopole ($\ell=3$), are especially important for studying the homogeneity and isotropy of the universe after the last scattering of the CMB photons (Maartens, Ellis & Stoeger 1996). The measurement of these low order multipoles requires observations over a large fraction of the sky, as provided initially by the COBE-DMR experiment, and more recently by the $WMAP^1$ satellite. The dipole is generally interpreted as being dominated by a kinetic effect related to the Earth's peculiar motion with respect to the CMB rest frame, so cosmologically relevant studies usually consider multipoles only from

the quadrupole upwards. The first measurement of the quadrupole by *COBE*-DMR suggested an intriguingly low value for its amplitude, and led to vigorous discussion about the credibility of its estimation (Smoot et al. 1992; Bennett et al. 1992; Stark 1993; Gould 1993; Kogut et al. 1996). In particular, doubts centred on limitations imposed by systematic effects, instrumental noise, and noncosmological foreground contributions due to local astrophysical emission. Nevertheless, the low amplitude of the quadrupole was another recently confirmed by high precision measurements from the *WMAP* satellite (Bennett et al. 2003a) after the application of a refined analysis of Galactic foreground contamination.

pointed Furthermore, as was by out Tegmark, de Oliveira-Costa and Hamilton (2003)(hereafter TOH) the quadrupole and octopole appear rather planar, with most of their hot and cold spots centred on a single plane in the sky. Moreover, the two planes appear rather aligned. All of these features could be explained by a specific non-standard topology for the universe. A broad class of finite universe models, including the Poincaré Dodecahedron model proposed by Luminet et al. (2003), was recently ruled out by Cornish et al. (2003). On the other hand, analysis of Slosar & Seljak (2004) strongly suggests that much of the alignment comes from the portion of the data most contaminated by Galactic foreground. Nevertheless, other studies have shown that there are also other intriguing correlations (Copi, Huterer & Starkman 2003; Schwarz et al. 2004) and anomalies (Eriksen et al. 2004b; Larson & Wandelt 2004; Vielva et al. 2003) of the low order WMAP multipoles.

The goal of this paper is to estimate the low order WMAP multipoles using a technique which allows the explicit determination of their reconstruction uncertainties, and subsequently to clarify whether the unexpected features of the quadrupole and octopole are significant.

2 THE PROBLEM

One of the major goals of the full sky measurements of the CMB radiation by satellite missions is to allow for the construction of a map of the anisotropy. To facilitate this, the measurements are discretized into $N_{\rm pix}$ pixels, which can be written as a $N_{\rm pix}$ -dimensional vector ${\bf y}$. This is related to the true CMB anisotropy field ${\bf x}$ by

$$\mathbf{y} = \mathbf{A}\mathbf{x} + \mathbf{n} \,, \tag{2}$$

where the matrix $\bf A$ encodes the effect of beam and pixel smoothing, while the additional term $\bf n$ represents the contribution from detector noise and foreground contamination. The foreground contamination can initially be minimized by masking out those regions of the sky with strong foreground emission, eg. due to the Galactic plane or point sources. The remainder of the map can then be corrected for the high latitude Galactic (and extragalactic if necessary) emission. The vector $\bf y$ then denotes such a cut sky, foreground corrected map and $\bf n$ its instrumental noise component.

In the spherical harmonic, $Y_{\ell m}$, space, the vector² of decomposition coefficients of the map on the cut sky, $\tilde{\mathbf{a}}$, is related to the corresponding vector on the full sky, \mathbf{a} , by

$$\tilde{\mathbf{a}} = \mathbf{W} \cdot \mathbf{A} \cdot \mathbf{a} + \mathbf{n}_c \,, \tag{3}$$

where \mathbf{n}_c denotes the noise vector on the cut sky and \mathbf{A} consists of the appropriate decomposition coefficients of the beam window function. We will assume that the beam profile is azimuthally symmetric. Then \mathbf{A} is a diagonal matrix dependent only on ℓ and consisting of the weights w_ℓ^{beam} . To simplify notation, hereafter \mathbf{a} will denote the vector multiplied by \mathbf{A} . \mathbf{W} is referred to as the coupling matrix and its (i, j)-th component is given by

$$W_{i(\ell,m),j(\ell',m')} = \int_{\text{cut skv}} Y_{\ell m}^*(\hat{\mathbf{n}}) Y_{\ell'm'}(\hat{\mathbf{n}}) d\Omega_{\hat{\mathbf{n}}} . \tag{4}$$

Our aim is to determine the full sky representation of the anisotropy written in terms of the coefficients **a** using the above relation. Unfortunately, we do not know the specific noise contribution, only a statistical description of the ensemble properties, and moreover the sky cut causes the coupling matrix **W** to be singular. This means that there is no information on those anisotropies that project onto modes in the spherical harmonic basis where the only structure lies within the sky cut. Hence it is impossible to reconstruct all of the modes from the $\tilde{\bf a}$. However, for low order multipoles, small sky cuts and a high signal-to-noise ratio, a good approximation is to simply truncate the vectors and coupling matrix at some value of the index $i(\ell,m)$ then reconstruct the multipole coefficients by inverting the non-singular truncated matrix **W**. This method was applied by to the first year WMAP data in Efstathiou (2003b), and will hereafter be referred to as direct inversion.

Direct inversion is a special case of a more general technique of estimation of the true sky signal by a linear transformation of the data vector $\tilde{\mathbf{a}}$

$$\hat{\mathbf{a}} = \mathbf{F} \cdot \tilde{\mathbf{a}} , \qquad (5)$$

where matrix **F** acts as a filter and satisfies certain conditions imposed on the solution $\hat{\mathbf{a}}$. In this paper, we will consider the application to our problem of both Wiener and power equalization filters, employing the methodology originally developed by Górski (1997) for *COBE*-DMR analysis.

2.1 Wiener filter

The Wiener filter is constructed from the requirement that the mean square deviation between the filtered, $\hat{\mathbf{a}}$, and the true signal, \mathbf{a} , $\epsilon = \left\langle (\hat{\mathbf{a}} - \mathbf{a})^T \cdot (\hat{\mathbf{a}} - \mathbf{a}) \right\rangle = \operatorname{tr} \left\langle (\hat{\mathbf{a}} - \mathbf{a}) \cdot (\hat{\mathbf{a}} - \mathbf{a})^T \right\rangle$, is minimized. Then we obtain

$$\mathbf{F}_W = \mathbf{S} \cdot \mathbf{W}^T \cdot \left(\mathbf{W} \cdot \mathbf{S} \cdot \mathbf{W}^T + \mathbf{N} \right)^{-1} , \qquad (6)$$

where $\mathbf{S} \equiv \langle \mathbf{a} \cdot \mathbf{a}^T \rangle$ and $\mathbf{N} \equiv \langle \mathbf{n}_c \cdot \mathbf{n}_c^T \rangle$ are covariance matrices of the signal and noise, respectively. One should notice that this filter practically annihilates those components of the data which are assessed to be noise dominated. Non-cosmological modes can be removed from the analysis by assumption that their power spectrum in the matrix $(\mathbf{W} \cdot \mathbf{S} \cdot \mathbf{W}^T + \mathbf{N})^{-1}$ is very large. In practise, the monopole and dipole are such terms, since for differencing experiments such as WMAP the monopole may correspond to an unphysical quantity related to the map-making process, whereas the dipole is attributed to the earth's motion in the universe. For negligible noise the filter is essentially equivalent to the direct inversion method and does not depend on the assumed signal covariance matrix. However, we would like to explicitly take into account the correlations induced by the cut between the lower order modes we are interested in reconstructing with the higher order modes present in the data. These correlations are non-negligible and play the role of noise in the Wiener filter.

² mapping from an index pair (ℓ, m) into a single index is described in appendix A

For further consideration, it will be useful to introduce a new orthonormal basis of functions on the cut sky. A method of construction such of such orthonormal functions, ψ , was proposed by Górski (1994). In appendix A more details are provided about these functions and the formalism used in the remainder of the paper.

In this new basis, the vector of decomposition coefficients of the cut sky map, \mathbf{c} , is related to vector \mathbf{a} by

$$\mathbf{c} = \mathbf{L}^T \cdot \mathbf{a} + \mathbf{n}_{tt} \,, \tag{7}$$

where **L** is the matrix derived by the Choleski decomposition of the coupling matrix and \mathbf{n}_{ψ} is the vector of noise coefficients in the ψ basis. Since **L** is a lower triangular matrix, **c** can be decomposed into a part dependent on both lower \mathbf{a}_{Γ} and higher $\mathbf{a}_{\mathcal{H}}$ order modes

$$\mathbf{c}_{\mathcal{L}} = \mathbf{L}_{\mathcal{L}\mathcal{L}}^T \cdot \mathbf{a}_{\mathcal{L}} + \mathbf{L}_{\mathcal{H}\mathcal{L}}^T \cdot \mathbf{a}_{\mathcal{H}} + \mathbf{n}_{\psi,\mathcal{L}}, \qquad (8)$$

and a part dependent only on higher order modes

$$\mathbf{c}_{\mathcal{H}} = \mathbf{L}_{\mathcal{H}\mathcal{H}}^T \cdot \mathbf{a}_{\mathcal{H}} + \mathbf{n}_{\psi,\mathcal{H}} . \tag{9}$$

The subscripts \mathcal{L} and \mathcal{H} denote the range of indices $i=1,\ldots,(\ell_{\rm rec}+1)^2$ and $i=(\ell_{\rm rec}+1)^2+1,\ldots,(\ell_{\rm max}+1)^2$ corresponding to those modes which are to be reconstructed with the filter (multipoles in the range from 1 to $\ell_{\rm rec}$) and the remainder of the modes used in the analysis (multipoles in the range from $\ell_{\rm rec}+1$ to $\ell_{\rm max}$), respectively. It should be noticed that only the first part of the vector \mathbf{c} contains information about lower order modes $\mathbf{a}_{\mathcal{L}}$, so to estimate them we will use only this part of the vector. This is a significant difference as compared to the vector $\tilde{\mathbf{a}}$ where information about the lower order modes is also contained in the second part, $\tilde{\mathbf{a}}_{\mathcal{H}}$.

Taking $\mathbf{c}_{\mathcal{L}}$ as a data vector, estimation of the lower order modes will be given by $\mathbf{\hat{a}}_{\mathcal{L}} = \mathbf{F} \cdot \mathbf{c}_{\mathcal{L}}$. For the Wiener filter we have³

$$\mathbf{F}_W = \mathbf{S}_{ff} \cdot \mathbf{L}_{ff} \cdot \mathbf{C}^{-1} \,, \tag{10}$$

where $\mathbf{C} = \mathbf{L}_{\mathcal{L}\mathcal{L}}^T \cdot \mathbf{S}_{\mathcal{L}\mathcal{L}} \cdot \mathbf{L}_{\mathcal{L}\mathcal{L}} + \mathbf{L}_{\mathcal{H}\mathcal{L}}^T \cdot \mathbf{S}_{\mathcal{H}\mathcal{H}} \cdot \mathbf{L}_{\mathcal{H}\mathcal{L}} + \mathbf{N}_{\psi}$ and $\mathbf{S}_{\mathcal{L}\mathcal{L}}$, $\mathbf{S}_{\mathcal{H}\mathcal{H}}$ are the appropriate covariance matrices of the CMB modes corresponding to the lower and higher multipoles, respectively. \mathbf{N}_{ψ} is the noise covariance matrix in the ψ -basis.

2.2 Power equalization filter

The power equalization (PE) filter is defined by the requirement that ${\bf F}$ is chosen such that

$$\langle \hat{\mathbf{a}} \cdot \hat{\mathbf{a}}^T \rangle = \mathbf{S}_{\mathcal{LL}}, \text{ i.e. } \mathbf{F}_{PE} \cdot \mathbf{C} \cdot \mathbf{F}_{PE}^T = \mathbf{S}_{\mathcal{LL}}.$$
 (11)

Using the Choleski decomposition of the relevant matrices, we can construct the power equalization filter as follows:

$$\mathbf{S}_{\mathcal{L}\mathcal{L}}^{-1} = \mathbf{L}_{\mathbf{S}_{\mathcal{L}\mathcal{L}}^{-1}} \cdot \mathbf{L}_{\mathbf{S}_{\mathcal{L}\mathcal{L}}^{-1}}^{T}, \qquad \mathbf{\Gamma}_{\mathbf{S}_{\mathcal{L}\mathcal{L}}^{-1}} = \mathbf{L}_{\mathbf{S}_{\mathcal{L}\mathcal{L}}^{-1}}^{-1}, \qquad \mathbf{S}_{\mathcal{L}\mathcal{L}} = \mathbf{\Gamma}_{\mathbf{S}_{\mathcal{L}\mathcal{L}}^{-1}}^{T} \cdot \mathbf{\Gamma}_{\mathbf{S}_{\mathcal{L}\mathcal{L}}^{-1}}, \quad (12)$$

$$\mathbf{C}^{-1} = \mathbf{L}_{\mathbf{C}^{-1}} \cdot \mathbf{L}_{\mathbf{C}^{-1}}^{T}, \quad \Gamma_{\mathbf{C}^{-1}} = \mathbf{L}_{\mathbf{C}^{-1}}^{-1}, \quad \mathbf{C} = \Gamma_{\mathbf{C}^{-1}}^{T} \cdot \Gamma_{\mathbf{C}^{-1}},$$
 (13)

and as a result we obtain an upper triangular matrix:

$$\mathbf{F}_{PE} = \mathbf{\Gamma}_{\mathbf{S}_{ff}^{-1}}^{T} \cdot \mathbf{L}_{\mathbf{C}^{-1}}^{T} , \qquad (14)$$

where the matrices $S_{\mathcal{LL}}$ and C are the same as in the Wiener filter

The condition (11) means that on average over many applications the power equalization filter renders filtered data whose statistically most likely power spectrum matches that of the

³ in appendix B the derivation using Bayes' theorem is shown

underlying signal. Since the PE filter is an upper triangular matrix, the non-cosmological monopole and dipole terms can be explicitly eliminated from the analysis. Then, the restored modes (with i > 4) are not contaminated by the monopole and dipole contributions.

2.3 Errors

The errors of estimation are determined on the basis of the diagonal terms of the covariance matrix, defined as $\mathbf{M} = \langle (\mathbf{a}_{\mathcal{L}} - \hat{\mathbf{a}}_{\mathcal{L}})(\mathbf{a}_{\mathcal{L}} - \hat{\mathbf{a}}_{\mathcal{L}})^T \rangle$. Thus, we have

$$\mathbf{M} = \left(\mathbf{F} \cdot \mathbf{L}_{\mathcal{L}\mathcal{L}}^{T} - \mathbf{I}\right) \cdot \mathbf{S}_{\mathcal{L}\mathcal{L}} \cdot \left(\mathbf{F} \cdot \mathbf{L}_{\mathcal{L}\mathcal{L}}^{T} - \mathbf{I}\right)^{T} + \\
+ \mathbf{F} \cdot \left(\mathbf{L}_{Hf}^{T} \cdot \mathbf{S}_{\mathcal{H}\mathcal{H}} \cdot \mathbf{L}_{\mathcal{H}\mathcal{L}}\right) \cdot \mathbf{F}^{T} + \mathbf{F} \cdot \mathbf{N}_{\psi} \cdot \mathbf{F}^{T},$$
(15)

where **I** is the identity matrix. This is a sum of three components: the first is due to correlations between the recovered low order multipoles, the second is induced by correlations with higher order multipoles and the last is generated by noise.

2.4 General considerations

In order to construct the filters we have to assume the form of both the signal and noise covariance matrices. We will make the usual assumption that both the CMB and noise components are Gaussian stochastic variables. The variances for individual modes of the CMB anisotropy, $C_\ell = \left\langle a_{\ell m}^2 \right\rangle$, are uniquely expressed as integrals over the power spectrum of the matter density fluctuations and depend only on ℓ due to the statistical isotropy of the CMB temperature field. The rms noise level in pixel p, $\sigma(p)_{\text{noise}} = \sigma_o / \sqrt{N_{\text{obs}}(p)}$, depends on quantities specific to a given instrument and scan strategy: the number of observations in pixel, $N_{\text{obs}}(p)$, and the rms noise per observation, σ_o . Dependence on the assumed power spectrum might seem to be disadvantage of these filtering methods. However, we will see that in the case of the *WMAP* data, the multipole estimation does not depend significantly on the assumed power spectrum.

3 DATA

The WMAP satellite observes the sky in five frequency bands denoted K, Ka, Q, V and W, centred on the frequencies of 22.8, 33.0, 40.7, 60.8 and 93.5 GHz, respectively. The maps are pixelized in the HEALPix⁴ scheme (Górski, Hivon & Wandelt 1998) with a resolution parameter $N_{\text{side}} = 512$, corresponding to 3,145,728 pixels with a pixel size of $\sim 7'$. The maps⁵ are corrected for the Galactic foreground using three templates – a radio survey at 408 MHz (Haslam et al. 1981), a H α map (Finkbeiner 2003a), and a dust map based on the combined COBE-DIRBE and IRAS data (Finkbeiner, Davis & Schlegel 1999) – to trace the synchrotron, free-free and dust emission. These are scaled to the WMAP frequencies using coefficients derived by fitting the templates to the data for the Kp2 sky coverage as described in Bennett et al. (2003b). For the O, V and W bands five coefficients are determined - an amplitude for each of the synchrotron and free-free components at 41 GHz (and scaled to the other frequencies by assuming spectral indices of -2.7 and -2.15 respectively), and three for the dust one at each frequency thereby including both the thermal and the

⁴ http://www.eso.org/science/healpix

⁵ available at http://lambda.gsfc.nasa.gov

anomalous dust component contributions. For the K and Ka channels, the coefficients from Table 3 of Bennett et al. (2003b) were used. The Q,V and W band maps are then combined using inverse-noise-variance weights to create the *corrected coadded map*.

We utilize several masks in the work which follows: the Kp2 mask (eliminating $\sim 15\%$ of the sky), the Kp0 mask (eliminating $\sim 23\%$ of the sky), an extended Galactic mask and mask '30'. The extended Galactic mask (hereafter denoted '20+') is the same as that used for the COBE-DMR data analysis and is defined as the region with latitude $|b| > 20^\circ$ plus custom cutouts in the vicinity of Orion and Ophiuchus (Bennett et al. 1996). The broadest mask '30' is defined as the region with latitude $|b| > 30^\circ$. The latter masks were additionally modified by excluding the point source mask included in the Kp2 and Kp0 masks, so that they finally eliminate $\sim 38\%$ and $\sim 50\%$ of the sky, respectively.

The WMAP multipoles will also be compared to those determined from the TOH cleaned and Internal Linear Combination (ILC, Bennett et al. 2003b) maps. Previous analyses have determined these multipole amplitudes on the full sky, however Eriksen et al. (2004a) have shown that residual Galactic foreground uncertainties for the ILC map in the Galactic plane are at the level of approximately 50 μ K. It is plausible that the TOH cleaned map can have errors of the same order. In what follows, we consider that the estimation of CMB anisotropy based on these maps is not credible when including this part of the sky, and we will omit the poorly reconstructed Galactic plane by using the same masks as for the WMAP corrected coadded map.

4 CHOICE OF ℓ_{MAX} AND ℓ_{REC}

The choice of $\ell_{\rm max}$ and $\ell_{\rm rec}$ is based on Monte Carlo (MC) simulations of the WMAP data, consisting of both realizations of the CMB anisotropy and noise. The CMB anisotropy maps were generated as random realizations of a Gaussian field with an angular power spectrum corresponding to the best fit ΛCDM cosmological model with running spectral index (Bennett et al. 2003a), convolved with the channel specific beam window function $w_\ell^{\rm beam}$. The noise maps were produced from Gaussian random numbers with pixel-dependent variance corresponding to the properties of the corrected coadded map. The simulated maps were studied after masking by the Kp2 mask.

The upper limit for possible values of ℓ_{max} and ℓ_{rec} is imposed by the feasibility of the Choleski decomposition of the coupling matrix. For a given cut, the coupling matrix becomes numerically singular for multipoles larger than $\ell_{Choleski}$ at which point the Choleski decomposition fails. For the Kp2 mask this multipole is found at $\ell_{Choleski} \sim 70$. The studies in this paper are focused mostly on estimation of the lowest multipoles ($2 \le \ell \le 10$), and particularly on those modes which have been shown to have potentially anomalous properties ($2 \le \ell \le 5$). Thus it is sufficient to include only multipoles up to $\ell_{max} = 30$. Increasing ℓ_{max} to 35 or 40 did not appreciably change the estimated values of these multipoles. This is a direct consequence of the decreasing amplitude of higher multipoles, scaling roughly as ℓ^{-1} ($\ell_{\ell} \propto \ell^{-2}$).

In order to establish a suitable value for ℓ_{rec} , 1000 MC simulations were generated and the PE filter computed with $\ell_{max}=30$ applied to the simulated maps masked by the Kp2 mask. The power spectrum of the difference between the true and restored multipole coefficients over the range $2 \le \ell \le 5$

$$C_{\ell}^{\text{error}} = \frac{\sum_{m=-\ell}^{\ell} \left\langle |a_{\ell m}^{\text{output}} - a_{\ell m}^{\text{input}}|^2 \right\rangle}{2\ell + 1},$$

is shown in Fig. (1) as a function of ℓ_{rec} . Notice that for $\ell_{rec}=\ell_{max}=30$ the errors are the largest. In this case, the PE filter does not adequately take into account the aliasing of higher order modes into the range $\ell \leq \ell_{rec}.$ Significant errors are seen also for lower values of $\ell_{rec},$ caused by correlations of the multipoles $\ell=2,\ldots,5$ with modes of order $\ell_{rec}+1,\ell_{rec}+2$ which for low values of ℓ_{rec} have significant amplitudes. In what follows we adopt $\ell_{rec}=10;$ although the flat power spectrum of the uncertainties over the range $10 \lesssim \ell_{rec} \lesssim 25$ allows a larger value for ℓ_{rec} to be selected, later in the paper we will consider the broader Galactic cut '30' for which the PE filter fails when too large a value for ℓ_{rec} is used.

It should be noted that other methods for the determination of the low multipoles also require the choice of some parameters to facilitate the reconstruction method. In particular, the direct inversion method of Efstathiou (2003a) adopts two parameters somewhat arbitrarily: the order of the multipole at which the coupling matrix is truncated and the FWHM of the beam for the initial smoothing of the data.

5 COMPARISON OF THE WIENER AND PE FILTERS

Fig. (2) provides a comparison of the *WMAP* power spectra obtained by the Wiener and PE filtering. In addition, we show the averages over 10,000 *WMAP* map simulations for the power spectra of the restored maps. In both cases the Kp2 mask and filters with $\ell_{\rm rec} = 10$, $\ell_{\rm max} = 30$ were applied.

The Wiener and PE filters differ mainly in the recovered power of the multipoles: there is a systematic suppression of power with increasing ℓ for maps reconstructed by the Wiener filtering. Conversely, the definition of the PE filter ensures an unbiased estimate for the multipole amplitudes. However, the PE filter does not give an optimal estimation in the minimum variance sense, i.e. an estimate which has the least variance between the true and restored data, which is the case for the Wiener filter case. Nevertheless, we decided to use PE filter in the remainder of the paper since for the lowest multipoles and Kp2 mask the results do not differ significantly from those derived by the optimal Wiener filter, and the unbiased nature of the estimator is considered to be more important. This is particularly relevant with increasingly aggressive sky cuts where the Wiener filter demonstrates even more suppression of power.

6 COMPARISON OF THE DIRECT INVERSION AND THE PE FILTERING METHODS

10,000 simulations of the *WMAP* data were again used to compare the accuracy of reconstruction of the low order multipoles by the direct inversion and the PE filtering methods. The reconstructions were performed for the Kp2 mask, and for a PE filter constructed with $\ell_{\rm rec}=10$ and $\ell_{\rm max}=30$. For the direct inversion method the coupling matrix was evaluated after truncation at either $\ell_{\rm rec}=10$ or 30. In both cases, following Efstathiou (2003a) the input map was smoothed by a Gaussian beam with FWHM=7°. Smoothing improves the accuracy of the direct inversion method reconstructions, since it damps higher order modes. The input and output (reconstructed) coefficients a_{ℓ} for the multipoles $\ell=2,\ldots,5$ are compared in Fig. (3) and Fig. (4). Only those modes with $m=\ell$ are shown since, as will be shown in Sect. 8.2, they (and the corresponding modes with $m=-\ell$) have the largest reconstruction uncertainties due to the removal of a large fraction

of their power by the cut. Thus, they are the most sensitive to the method used in their estimation. Nevertheless, comparison of the other modes gives qualitatively similar results.

Fig. (3) shows that the PE filter recovers the quadrupole and octopole amplitudes with a similar accuracy to the direct inversion method. However, for higher order modes, the PE filter is superior. This does not appear to be connected to the use of $\ell_{\rm rec}=10$ for the direct inversion method; increasing this value to $\ell_{\rm rec}=30$ yields even worse reconstructions (Fig. (4)). The higher accuracy of the PE filter reconstructions is a consequence of explicitly accounting for the aliasing of higher order multipoles into the lower multipole range in the filter construction.

7 APPLICATION TO THE WMAP DATA

The PE filter was applied to WMAP maps with $\ell_{max} = 30$ and $\ell_{rec} = 10$. We are mostly interested in the analysis of the lowest multipoles $\ell = 2, \ldots, 5$ since these are the most sensitive to the cut and foreground emission. The monopole and dipole were not restored since they do not provide any relevant cosmological information. In order to construct the filter matrix, the WMAP best fit ΛCDM model ($\Omega_{\Lambda} = 0.73$, $\Omega_{m} = 0.27$) with a running primordial spectral index⁶ (Bennett et al. 2003a) was used. This choice is based on the fact that the spectrum provides a better fit to the WMAP data on large angular scales compared to a simple power law spectrum. However, tests with a power law spectrum yields similar results. The noise covariance matrices were constructed in the usual fashion, with pixel variances determined by the number of observations $N_{obs}(p)$ in pixel p as provided by WMAP team.

The power spectrum will provide a useful complement to the studies of the multipole maps. We will use an estimator of the power spectrum given by

$$\hat{C}_{\ell} = \frac{\sum_{m=-\ell}^{\ell} |\hat{a}_{\ell m}|^2}{2\ell + 1} , \tag{16}$$

where $\hat{a}_{\ell m}$ denotes the restored harmonic coefficients. The definition of the PE filter ensures that the estimator is unbiased. Given the error covariance matrix \mathbf{M} , one can estimate the uncertainty in the quantity $\hat{\mathcal{C}}_{\ell}$ by

$$\sigma_{\ell}^{2} = \frac{2}{(2\ell+1)^{2}} \sum_{m,m'=-\ell}^{\ell} \mathbf{M}_{ij} \left(2\hat{a}_{i} \hat{a}_{j} - \mathbf{M}_{ij} \right) , \qquad (17)$$

where the indices i, j in ℓ -ordering are expressed by $i = \ell^2 + \ell + m + 1$. This estimation of the uncertainty takes into account only errors induced by the sky cut and noise; it does *not* take into account cosmic variance related errors which enter through the assumption of a cosmological power spectrum to build the PE filter. Table (1) indicates the reconstruction accuracy of the method.

7.1 The multipoles maps

Maps of the recovered multipoles computed from the *WMAP* corrected coadded map are compared to the multipoles of the TOH cleaned and ILC maps in Fig. (5). Since the details of the noise model are essentially negligible for the estimation of low order multipoles, we have used the same PE filter as for the corrected

Table 1. Rms difference between the true and estimated power spectra C_{ℓ}^{error} (in μK^2) and the correlation coefficients $r_{\ell\ell}$ of the ℓ -order, $m=\ell$ modes estimated from a set of 10,000 simulations of the *WMAP* data analysed after application of the Kp2 mask. In the third column, the signal to error ratio is shown where \hat{C}_{ℓ} is the estimated power spectrum of the *WMAP* multipoles maps given by PE filtering.

ℓ	$C_\ell^{ m error}$	$\hat{C}_\ell/C_\ell^{\rm error}$	$r_{\ell\ell}$
2	69	2.8	0.99
3	41	12	0.98
4	26	9.6	0.97
5	19	17	0.96
6	14	5.2	0.94
7	12	11	0.92
8	9.0	6.3	0.90
9	7.6	7.6	0.87
10	6.2	7.3	0.84

coadded map for the TOH and ILC maps. The comparison confirms previous the results of estimations of the multipole amplitudes. Small discrepancies are seen only at $\ell=2$, where the hot spots are closer to the Galactic equator and the amplitude is smaller for our results. The power spectrum of the maps is shown in Fig. (6) and summarised in table (2). The cut sky analysis of Hinshaw et al. (2003) shows substantially less power at $\ell=3,5$ and 7 than for the other estimates. Efstathiou (2003a) has claimed that this is a consequence of the quadratic nature of this estimator. Our linear estimator results, and in particular the ILC results in table (2), are in good agreement with those of Efstathiou (2003a).

7.2 Dependence on the assumed angular power spectrum

Since construction of the filters requires some assumption about the CMB anisotropy power spectrum C_ℓ , one should investigate how sensitive the amplitudes of the restored multipoles are to this choice and thus quantify the uncertainties in the amplitudes related to the assumption. To answer these questions we have applied filters constructed using two other power spectra: the canonical one described above but with the square root of the cosmic variance either added or subtracted. In Fig. (7) we see that the power spectrum of the resultant maps is changed only weakly by these perturbations, up to few percent. For the *WMAP* analysis presented here, the PE filtering method gives robust estimates of the amplitudes of the low order multipoles, essentially independent of the assumed input power spectrum.

7.3 Dependence on frequency

Comparison of the multipoles maps determined from the foreground corrected WMAP data frequency-by-frequency allows us to determine the extent to which the derived structures are cosmological, and the degree of residual foreground contamination. In Fig. (8) it is seen that the foreground cleaning of the K-band map gives the worst results. The multipole maps differ substantially from the rest of the maps showing excess of the power near the Galactic plane. Nevertheless, apart from the quadrupole, there is a qualitative similarity in the distribution of hot and cold spots relative to the other frequency channels. In particular, the octopole is planar with approximately the same preferred axis, along which the power is suppressed, for all frequencies. The quadrupole is also planar, although changes of the plane are more pronounced, especially for the K and Ka bands. Small deviations between the Q, V and W bands indi-

⁶ available at http://lambda.gsfc.nasa.gov

Table 2. Power spectrum amplitudes $\Delta T_{\ell}^2 = \ell(\ell+1)C_{\ell}/2\pi$ (in μK^2) for the foreground corrected *WMAP* frequency maps and related combinations estimated by application of the PE filter for the Kp2 sky coverage. Q+V+W denotes the corrected coadded map and * denotes estimation on the full sky. The direct inversion method was applied to the corrected coadded map for the Kp2 mask. Uncertainties do not take into account cosmic variance.

	ΔT_2^2	ΔT_3^2	ΔT_4^2	ΔT_5^2	ΔT_6^2	ΔT_7^2	ΔT_8^2	ΔT_9^2	ΔT_{10}^2
K	963 ± 79	1710 ± 160	3290 ± 220	2070 ± 130	710 ± 110	1060 ± 120	1320 ± 120	1330 ± 150	1680 ± 180
Ka	176 ± 26	1060 ± 120	1190 ± 110	1550 ± 110	312 ± 55	960 ± 100	786 ± 84	920 ± 130	1100 ± 140
Q	158 ± 32	990 ± 110	875 ± 80	1610 ± 120	459 ± 77	1100 ± 110	683 ± 75	880 ± 130	840 ± 120
V	206 ± 40	930 ± 100	755 ± 63	1600 ± 120	523 ± 79	1070 ± 110	644 ± 69	800 ± 130	750 ± 110
W	219 ± 42	910 ± 100	804 ± 67	1580 ± 130	553 ± 79	1110 ± 120	645 ± 69	780 ± 130	770 ± 110
Q+V+W	182 ± 36	950 ± 110	804 ± 70	1600 ± 120	491 ± 78	1090 ± 110	656 ± 71	830 ± 130	790 ± 110
Direct inversion	322 ± 36	873 ± 96	1530 ± 120	1370 ± 110	569 ± 78	870 ± 100	1037 ± 99	950 ± 140	1090 ± 130
ILC	248 ± 45	950 ± 110	750 ± 61	1620 ± 130	615 ± 85	1120 ± 120	619 ± 66	790 ± 130	639 ± 98
TOH	279 ± 49	870 ± 98	613 ± 49	1420 ± 110	586 ± 89	1040 ± 110	631 ± 63	860 ± 140	760 ± 110
ILC*	195 ± 40	1050 ± 110	834 ± 66	1670 ± 130	606 ± 81	1290 ± 140	660 ± 68	700 ± 130	780 ± 110
TOH*	202 ± 41	866 ± 99	651 ± 50	1350 ± 110	608 ± 90	1010 ± 110	681 ± 72	710 ± 120	890 ± 120

cates that, after foreground cleaning, these maps are dominated by the CMB anisotropy component and can be treated as a reliable picture of the CMB multipoles.

The corresponding power spectra shown in Fig. (9) and summarised in table (2) clearly show that the applied foreground correction does not remove all the contamination for the K and (partially) Ka bands. This suggests that the Kp2 cut is not sufficient to remove the strong signals near to the Galactic plane at those frequencies (despite the fact that the Kp2 mask is derived from considerations of the thresholded temperature distribution of the Kband map). The strong synchrotron and free-free emission extends to higher Galactic latitudes at these lower frequencies.

7.4 Dependence on the sky cut

More substantial changes of the multipoles are seen with then application of more aggressive sky cuts. In Fig. (10) we show the multipoles determined from the WMAP corrected coadded data after masking by the Kp2, Kp0, '20+' and '30' masks. All multipoles lose their characteristic features for mask '30'. Nevertheless, up to sky cut '20+' the multipoles $\ell = 3$ and $\ell = 5$ do not change significantly. The multipoles $\ell = 2$ and $\ell = 4$ are more sensitive to the mask and change substantially even for smaller cuts.

The corresponding power spectra are presented in Fig. (11) and table (3). It should be noticed that generally the uncertainties increase rapidly with the width of the sky cuts. Because our estimation of the errors (17) depends on the multipole power, the few exceptions from this rule $-\ell = 6$ for the '20+' mask, $\ell = 7, 8, 9$ for the '30' mask – are a consequence of the substantially lower amplitudes of the multipoles estimated in those cases. Notice that for very low power, the estimation of the square of the error can be negative. Since we have such a situation for the quadrupole estimated for the cut '30', we do not quote the corresponding uncertainties in the table.

The general trend for increasing uncertainties with increasing sky cut is easily seen in Fig. (12) where linear regressions, analogous to that in Sect. 6, is shown for various masks. It should be noticed that uncertainties in the estimation of the multipoles $\ell = 4, 5$ is especially large for the cut '30'. The true and reconstructed coefficients are nearly uncorrelated. Slightly better correlations are seen for modes with $m \neq -\ell, \ell$, though the trend is still maintained. The poor correlation between input and recovered coefficients implies that for $\ell > 5$ their estimation is no longer credible. Indeed, the large uncertainties associated with the widest cut '30' helps to explain why the appearance of the estimated WMAP multipoles is dif-

Table 3. Power spectra of the multipoles $\Delta T_{\ell}^2 = \ell(\ell+1)C_{\ell}/2\pi$ (in μK^2) estimated by the PE filtering after applying various masks. Uncertainties do not take into account cosmic variance.

		Mask					
		Kp2	Kp0	'20+'	'30'		
	$\ell = 2$	182 ± 36	294 ± 88	200 ± 130	77		
	$\ell = 3$	950 ± 110	870 ± 170	890 ± 310	830 ± 380		
	$\ell = 4$	804 ± 70	723 ± 94	970 ± 280	790 ± 310		
	$\ell = 5$	1600 ± 120	1470 ± 170	820 ± 280	980 ± 450		
ΔT_{ℓ}^2	$\ell = 6$	491 ± 78	480 ± 110	200 ± 54	690 ± 260		
·	$\ell = 7$	1090 ± 110	1110 ± 190	1460 ± 380	700 ± 240		
	$\ell = 8$	656 ± 71	750 ± 130	920 ± 250	560 ± 130		
	$\ell = 9$	830 ± 130	780 ± 180	860 ± 250	750 ± 220		
	$\ell = 10$	790 ± 110	610 ± 140	590 ± 140	730 ± 170		

ferent from that estimated with narrower masks. Nevertheless, the multipole amplitudes remain statistically consistent over the range of masks at approximately the two standard deviation level.

UNCERTAINTIES OF THE MULTIPOLES MAPS

One of the merits of the PE filtering method is the possibility to directly estimate the uncertainties in the derived results, and the preservation of the well-defined noise properties of the original maps. This is a clear advantage of the method over the Maximum Entropy Method (MEM, Hobson et al. 1998) which results in anisotropy maps with complex noise properties which are largely inappropriate for most CMB analyses. Here we derive errors both in pixel and spherical harmonic space.

8.1 The maps of the standard deviation

To study the spatial distribution of the uncertainties of the restored multipole maps we use the simulations of the WMAP corrected coadded map as described in Sect. 4. The map

$$\Delta^{2}(p)_{\text{error}} = \sum_{\ell_{1}, m_{1}} \sum_{\ell_{2}, m_{2}} \left\langle a_{\ell_{1}, m_{1}}^{\text{error}} a_{\ell_{2}, m_{2}}^{\text{error}} \right\rangle Y_{\ell_{1}, m_{1}}(p) Y_{\ell_{2}, m_{2}}(p) , \qquad (18)$$

shows the spatial distribution of the squared standard deviation of the difference between the restored and true multipole maps. $a_{\ell_1,m_1}^{\text{error}}$ are the corresponding decomposition coefficients of the difference

maps and terms $\langle a_{\ell_1,m_1}^{\rm error} a_{\ell_2,m_2}^{\rm error} \rangle$ are averaged over 10,000 simulations. Using the identity

$$\begin{array}{lcl} Y_{\ell_1,m_1}(p)Y_{\ell_2,m_2}(p) & = & \displaystyle \sum_{\ell,m} \sqrt{\frac{(2\ell_1+1)(2\ell_2+1)(2\ell+1)}{4\pi}} \times \\ & & \left(\begin{array}{ccc} \ell_1 & \ell_2 & \ell \\ m_1 & m_2 & m \end{array} \right) \left(\begin{array}{ccc} \ell_1 & \ell_2 & \ell \\ 0 & 0 & 0 \end{array} \right) Y_{\ell,m}(p) \; , \end{array}$$

where $\begin{pmatrix} \ell_1 & \ell_2 & \ell \\ m_1 & m_2 & m \end{pmatrix}$ is the Wigner 3j symbol, the expression (18) can be written as

$$\Delta^{2}(p)_{\text{error}} = \sum_{\ell,m} b_{\ell,m} Y_{\ell,m}(p) ,$$

where $b_{\ell,m}$ are the appropriate coefficients. The Δ^2_{error} map is composed of modes $0 \le \ell \le 2\ell_1$, because ℓ obeys the triangular condition $(\ell = \ell_1 + \ell_2, \ell_1 + \ell_2 - 1, \dots, |\ell_1 - \ell_2|)$ and $\ell_1 = \ell_2$.

The Δ^2_{error} maps, computed for the Kp2 mask are shown in Fig. (13) in logarithmic scale. As expected, due to the lack of the data in the cut part of the sky the reconstructed multipoles have the largest uncertainties in this region, especially close to the Orion and Ophiuchus exclusion zones. The multipoles $\ell = 2$ and 3 have the smallest uncertainties inside the cut. This is a consequence of the fact that the multipole maps characterize the CMB anisotropy on angular scales $\sim 1/\ell$. If this is bigger than the angular width, $\Delta\theta$, of the mask then the excised region of the multipole map can be easily extrapolated from the data outside of the cut. Otherwise, there will be fluctuations with typical angular size smaller than $\Delta\theta$, which will be completely contained within the cut and their reconstruction from the data will be much less accurate. The statistical isotropy assumption used in our approach is then very helpful to reduce uncertainties in these cases. For the Kp2 mask, the widest part, cutout toward the Galactic centre, has width $\Delta\theta \approx 40^{\circ}$.

The Δ^2_{error} map corresponding to the sum of the multipoles $\ell=2,\ldots,5$ shows much bigger uncertainties than for the corresponding individual multipoles. This is due to the additional contributions from the correlations between errors in the multipoles. These correlations are easily seen in the covariance matrix \mathbf{M} .

8.2 The covariance matrix

The map of the standard deviation does not show all of the information about the errors. The covariance matrix **M** shows that the uncertainties are correlated in the spherical harmonic space.

As mentioned in Sect. 2, the covariance matrix, M, consists of three components: the noise component and, induced purely by the cut, contributions from correlations between the restored multipoles and correlations with higher order multipoles. In Fig. (14) we show that part of the covariance matrix corresponding to the multipoles $\ell = 2, \dots, 5$ for the PE filtering of the WMAP corrected coadded map, together with the corresponding sub-matrices for the separate components. The largest contribution arises from correlations with higher order modes. The correlations between the low order reconstructed multipoles are weaker although still non-negligible. The smallest contribution comes from the noise component, which is plotted multiplied by a factor of 50 to render it visible. The approximately axisymmetric cut causes stronger correlations between modes with ℓ -value different by 2. Notice that the modes with the biggest reconstruction uncertainties are for $m = -\ell$ and $m = \ell$, which is a consequence of removing a large fraction of the power of these modes, mainly concentrated in the Galactic plane, by the cut

9 FOREGROUND SEPARATION

In this section, we will reconsider the sensitivity of the estimated CMB multipoles to the Galactic foregrounds. To achieve this, we derive a CMB anisotropy map by the decomposition of the multi-frequency *WMAP* data by making assumptions about the frequency dependence of the foreground components. The advantage of this method is that, unlike with the template fits of Bennett et al. (2003b), we assume nothing about the morphological distribution of the foreground emission. Thus foregrounds which are not well traced by the existing templates, but with similar spectra, eg. the free-free haze proposed by Finkbeiner (2003a), are taken into account. The disadvantage is that, to separate the components properly, we need to know their spectral dependence. Given the high signal-to-noise content of the *WMAP* data on the large angular scales of interest here, we consider the following simple method.

We suppose now that we observe the sky in m different frequency channels, so that at each point \mathbf{r} on the sky we measure m different temperatures $y_i(\mathbf{r})$, $i=1,\ldots,m$. Let us assume also that we know the temperature spectra $f_j(v)$ of all n components $x_j(\mathbf{r})$, $j=1,\ldots,n$. Then we can write

$$\mathbf{y}(\mathbf{r}) = \mathbf{F} \cdot \mathbf{x}(\mathbf{r}) + \mathbf{n}(\mathbf{r}) , \qquad (19)$$

where the vector $\mathbf{n}(\mathbf{r})$ corresponds to the instrumental noise in the various channels, and \mathbf{F} (not to be confused with the filter matrix used in the previous context) is $m \times n$ frequency response matrix given by

$$F_{ij} \equiv \int_0^\infty w_i(\nu) f_j(\nu) d\nu , \qquad (20)$$

 $w_i(v)$ being the frequency response of the *i*th channel. Here, we will approximate $w_i(v)$ by Dirac's delta $w_i(v) = \delta(v - v_i)$ where v_i corresponds to the mean frequency in the *i*th channel, so that $F_{ij} = f_i(v_i)$. If the number of frequencies, m, equals the number of components n and noise is negligible, the separation of the components can be obtained by inverting the frequency response matrix, $\mathbf{x}(\mathbf{r}) = \mathbf{F}^{-1}\mathbf{y}(\mathbf{r})$. For the CMB component $F_{i1} = 1$ (if temperature is expressed in thermodynamic units) for all frequencies due to the blackbody nature of the spectrum. Over the range of frequencies of interest here, the foreground spectra may be reasonably well modelled by a power law in antenna temperature, $f_i(\nu) \propto \nu^{\beta_j}$, where the spectral index β_i depends on the component. To express the spectral dependence in thermodynamic units, the function $f_i(v)$ must include the frequency dependent antenna to thermodynamic temperature conversion factor, $d_{\text{ant to therm}}(v)$. Thus, finally the functions take the form $f_j(\nu) = d_{\text{ant to therm}}(\nu) \left(\nu/\nu_{0,j}\right)^{\beta_j}$, where $\nu_{0,j}$ is the reference frequency for component j at which the foreground amplitude

For the WMAP data, maps are measured at 5 frequencies: K, Ka,Q, V, and W bands (i = 1, ..., 5, respectively) and these may be interpreted as consisting of 5 components: the CMB anisotropy, Galactic thermal dust, synchrotron, free-free and "anomalous dust" emissions (j = 1, ..., 5, respectively).

The synchrotron, free-free and anomalous dust components will be searched at K-band frequency $v_{0,s} = v_{0,ff} = v_{0,a} = 23$ GHz and the thermal dust component at W-band frequency $v_{0,d} = 94$ GHz. It should be recognised that the Galactic emission does in general have spectral properties that depend on position on

the sky (especially in the the Galactic plane), however we will neglect these variations and use a fixed index over the high latitude parts of the sky we are interested in. This is no different to the assumption that the template fits can be described by single scale factors. Note that, before proceeding with the separation, the *WMAP* maps were smoothed to common resolution 1°.

For the spectral indices of the components, we have considered a broad range of values in order to aggressively test the dependence of the low order multipoles to these assumptions. For the thermal dust component the spectral index generally lies in the range 1.6 $\lesssim \beta_d \lesssim$ 2.5 (Dupac et al. 2002). Three values were selected: $\beta_d = 1.7$ suggested by Finkbeiner et al. (1999), $\beta_d = 2.2$ which is the mean value of the index determined from the MEMfit dust component derived from the WMAP data by Bennett et al. (2003b), and the upper limit of the range $\beta = 2.5$. The synchrotron spectral index is negative and again three values were selected: $\beta_s = -3.3$ which approximately corresponds to the mean spectral index between the Ka and Q bands of the WMAP MEM-fit synchrotron component, $\beta_s = -3.1$ which is a better fit to the Galactic halo emission, and $\beta_s = -2.9$ more appropriate for the Galactic plane. The spectral dependence of the so-called anomalous dust component was studied by Banday et al. (2003). Over the frequency range 19 - 90 GHz, the anomalous dust has a thermal dust-like morphology but a synchrotron-like spectrum with an index $\beta_a \approx -2.5$. Unfortunately, the similarity of the latter two spectra results in the the frequency response matrix becoming poorly conditioned and the clean separation of the components is not possible. To sidestep this issue, we adopted the "spinning" dust model spectrum proposed by Draine & Lazarian (1998). Nevertheless, further degeneracy in the components caused by the similarity of the freefree spectral $\beta_{ff} \approx -2.15$ and the synchrotron indices, renders it impossible to perform a robust separation of all 5 components. We have to eliminate the free-free or synchrotron component from the linear system. Since the former is better known (in the sense that there are less variations in the spectral index over the sky) and of lesser contribution to the foreground signal, we adopt a free-free template to describe its spatial morphology and subtract it from the 5 temperature maps, y(r), with the correlation coefficients derived by Bennett et al. (2003b) (table 3). However, a major uncertainty when using the H α template is the absorption of the H α by foreground dust. To study the sensitivity of the lowest multipoles to the dust absorption correction we will use two templates of the free-free emission: $H\alpha$ template given by Finkbeiner (2003a) (it was used by Bennett et al. 2003b) uncorrected for dust absorption and $H\alpha$ template corrected for dust absorption given by Dickinson, Davies & Davis (2003). Unfortunately, dust may not be the only problem in removing free-free emission. Finkbeiner (2003b) has suggested that the H α map does not trace all of the free-free emission, and proposed the existence of a so-called freefree "haze" which has the same spectral dependence as free-free component. The influence of the free-free haze on the estimation of the lowest multipoles will be studied using maps corrected and uncorrected for this component.

After elimination of the free-free component, an overdetermined linear system of 5 equations and 4 unknowns remains to be solved. This is performed using the Singular Value Decomposition (SVD) method, since it gives the minimum variance solution. Then, the PE filter was applied to the derived CMB component maps. Residuals associated with poorly subtracted Galactic plane emission were circumvented by application of the Kp2 mask.

The influence of the dust absorption and free-free haze corrections on the lowest *WMAP* multipoles is shown in Fig. (15). The

dust and synchrotron spectral indices were fixed here as $\beta_d = 2.2$ and $\beta_s = -3.1$, respectively. One can see that quadrupole is especially sensitive to these corrections. The dust absorption correction shifts the hotter spots of the quadrupole toward the Galactic poles and the free-free haze correction shifts the spots toward the Galactic plane. Curiously, when both corrections are applied, the quadrupole remains largely unchanged. Notable changes are seen also for the $\ell = 4$ multipole, but the results for $\ell = 3$ and 5 are very stable with respect to the corrections.

The dependence of the $\ell=2$ multipole on the thermal dust and synchrotron spectral indices is shown in Fig. (16). We do not show analogous figures for $\ell=3,4,5$ since they remain unperturbed ($\ell=3,5$) or show minimal changes ($\ell=4$) with respect to the spectral indices. It should be noted that an increase in the synchrotron spectral index tends to shift the hot spots of the quadrupole toward the Galactic poles and enhance its amplitude. Conversely, increasing the dust spectral index shifts the spots toward the Galactic plane and decreases their amplitude. Thus, for the flattest dust $\beta_d=1.7$ and synchrotron $\beta_s=-2.9$ indices, the quadrupole hot spots are at the Galactic poles. Similar changes though much smaller are also seen for multipole $\ell=4$.

The stability of the multipoles $\ell=3$ and $\ell=5$ with respect to the spectral indices, combined with the earlier results related to the removal of the free-free template, is compelling evidence in favour of the claim that the planarity of the octopole is not caused by the Galactic foregrounds. Conversely, the strong dependence of the quadrupole amplitude and morphology on the spectral properties of the Galactic foreground emission implies that the latter must be known in some detail in order to recover the quadrupole anisotropy with some degree of precision. Indeed, this will also have important consequences for the statistical significance of its alignment with octopole. This issue is studied in next section.

10 THE QUADRUPOLE AND OCTOPOLE PREFERRED AXES

As initially noticed by de Oliveira-Costa et al. (2003), and seen here in Fig. (5), the quadrupole and octopole are rather planar, with most of their hot and cold spots placed on a single plane in the sky. de Oliveira-Costa et al. (2003) use a wave function formalism to quantify a preferred axis for the multipoles and study the significance of their alignment. However, their analysis was based on the full sky TOH map which may contain residual contamination in the Galactic plane region. We repeat the analysis here on the multipoles derived from the cut sky analysis (thus avoiding this problem), and quantify the additional statistical uncertainties introduced by the mask.

Given the covariance matrix **M** we can estimate uncertainties of the preferred axes coordinates on the sky. For each of the masks: Kp2, Kp0 and '20+' the covariance matrix **M** was used to perform 100 constrained realizations of the *WMAP* quadrupole and octopole. Then, using the same technique as de Oliveira-Costa et al. (2003) the preferred axis for each of the multipoles was found. The uncertainties in the axis coordinates are summarised in table (4). Notice that the multipoles axes coordinates substantially vary for different masks. The most changeable is the quadrupole, particularly in latitude, whereas the octopole axis coordinates are much more robust.

Table (5) indicates the frequency dependence of the preferred axis for the quadrupole and octopole. One should notice that the best foreground corrected octopole maps (those of the Q, V and W

Table 4. Galactic coordinates of the quadrupole and octopole axes for different masks.

		Kp2	Kp0	'20+'
$\ell = 2$	longitude	273° ± 8°	298° ± 5°	276° ± 53°
	latitude	$68^{\circ} \pm 3^{\circ}$	$40^{\circ} \pm 16^{\circ}$	$34^{\circ} \pm 28^{\circ}$
$\ell = 3$	longitude	$307^{\circ} \pm 4^{\circ}$	$301^{\circ} \pm 6^{\circ}$	$267^{\circ} \pm 22^{\circ}$
	latitude	$63^{\circ} \pm 2^{\circ}$	$62^{\circ} \pm 3^{\circ}$	$66^{\circ} \pm 9^{\circ}$
angle b	etween axes	15°	22°	32°

Table 5. Galactic coordinates of the quadrupole and octopole axes for different frequencies. In all cases the multipoles were derived from input maps where the Kp2 mask was applied. The coordinates have uncertainties as in table (4).

		K	Ka	Q	V	W
$\ell = 2$	longitude	107°	228°	262°	282°	280°
	latitude	1°	29°	66°	63°	71°
$\ell = 3$	longitude	299°	312°	310°	307°	306°
	latitude	74°	69°	65°	63°	62°
angle between axes		105°	61°	19°	11°	14°

bands) are stable and prefer approximately the same axis: $(l,b) \sim (308^\circ, 63^\circ)$ with a deviation of order two degrees. The quadrupole axis is more poorly determined. Significant differences between the Q, V, W and K, Ka frequency bands suggest the presence of residual foregrounds at the lowest frequencies.

As was shown in Sect. 9 the quadrupole of the CMB map derived by the linear projection depends significantly on templates used to eliminate the free-free emission and assumptions concerning the spectral dependence of the dust and synchrotron emission. The coordinates of the quadrupole and octopole preferred axes for variants of the free-free model emission are shown in table (6). Again, the octopole is much more stable than the quadrupole. Correction for the putative free-free haze emission shifts the quadrupole axis toward the Galactic plane (higher latitude), and the dust absorption correction toward the Galactic poles (smaller latitude).

The octopole axis is also stable and does not change for different spectral indices of the dust and synchrotron emission. For all

Table 6. Galactic coordinates of the quadrupole and octopole axes for four variants of the free-free emission correction of the *WMAP* maps (see text). Columns (1), (2), (3) and (4) correspond to, respectively: no free-free haze correction and no dust absorption correction, free-free haze correction and dust absorption correction, no free-free haze correction and dust absorption correction, free-free haze correction and dust absorption correction. The dust and synchrotron spectral indices are $\beta_d=2.2$ and $\beta_s=-3.1$, respectively.

		no dust corr		dust corr	
		(1)	(2)	(3)	(4)
$\ell = 2$	longitude	297°	290°	300°	295°
	latitude	48°	66°	27°	56°
$\ell = 3$	longitude	306°	301°	301°	299°
	latitude	62°	62°	62°	60°
angle between axes		15°	6°	35°	5°

Table 7. Galactic coordinates of the quadrupole axes for various spectral indices of the dust and synchrotron emission. The first number in brackets is longitude and the second latitude. In all cases the maps were masked by Kp2 mask, thus the coordinates have uncertainties the same as in table (4) for Kp2 mask.

			$eta_{ m synch}$	
		-3.3	-3.1	-2.9
$eta_{ m dust}$	1.7 2.2 2.5	(297°, 48°) (292°, 63°) (285°, 68°)	(297°, 33°) (295°, 56°) (295°, 60°)	(297°, 19°) (297°, 36°) (296°, 47°)

studied indices it is $(l, b) = (299^{\circ}, 60^{\circ})$. The quadrupole axis, as in previous cases, is much less stable (see table (7)).

In summary of this section it is worth emphasizing that the above results show a much better determination of the octopole and its preferred axis than for the quadrupole. Significant uncertainties of estimation for the quadrupole preferred axis and its strong dependence on the details of templates used to eliminate free-free emission and foreground spectral indices must increase the low probability of the *WMAP* quadrupole-octopole alignment estimated by de Oliveira-Costa et al. (2003). The importance of quantifying errors due to the foreground subtraction should be clear.

11 APPLICATION TO THE COBE-DMR DATA

As a useful cross-check, in particular against systematic effects, we investigate whether the lowest order multipole maps derived from *COBE*-DMR are consistent with the *WMAP* results. We treated the *COBE*-DMR data in similar way to the *WMAP* data. Firstly, we corrected the maps for the Galactic foreground using the '20+' mask and the Galactic emission templates as was described in Górski et al. (1996) and then coadded the 53 and 90 GHz maps using inverse-noise-variance weights. The 31.5 GHz data were not used since under such a weighting scheme the contribution of these least sensitive maps is minimal. The PE filter was constructed using the best fit to the data power spectrum parameterized by (Bond & Efstathiou 1987, Fabbri, Lucchin & Matarrese 1987)

$$C_{\ell} \equiv \left\langle a_{\ell,m}^{2} \right\rangle = Q_{rms-PS}^{2} \frac{4\pi}{5} \frac{\Gamma(\ell + \frac{n-1}{2})\Gamma(\frac{9-n}{2})}{\Gamma(\ell + \frac{5-n}{2})\Gamma(\frac{3+n}{2})} , \tag{21}$$

where Γ denotes the gamma function. The rms quadrupole normalisation Q_{rms-PS} and spectral index n were estimated in Górski et al. (1996) – $Q_{rms-PS}=15.3^{+3.7}_{-2.8}~\mu\text{K}$, $n=1.2\pm0.3$, and we used the values of the parameters which maximize the likelihood function The noise covariance matrix was estimated analogously to the WMAP matrix. ℓ_{rec} and ℓ_{max} were the same as for the WMAP PE filter.

The *COBE*-DMR and *WMAP* multipoles maps for the same '20+' mask are compared in Fig. (17). One sees that the maps are similar. The *COBE*-DMR octopole appears to be planar like the *WMAP* octopole and prefers roughly the same axis, in the direction of $(l,b) \sim (277^{\circ},63^{\circ})$. The hot spots of the *COBE*-DMR quadrupole are shifted more toward the Galactic poles than the spots of the *WMAP* quadrupole, which may reflect differences in the foreground removal.

10 *I*

12 SUMMARY

In this paper, we have re-examined the nature of the low order multipoles derived from the *WMAP* data. Previous work has suggested that these modes demonstrate unusual properties, but such results have been derived from full sky analyses of maps of the CMB anisotropy derived by methods which are susceptible to residual Galactic foregrounds (Eriksen et al. 2004a), particularly in the Galactic plane. By application of a PE filter on the cut sky we circumvent these difficulties, and have estimated the amplitudes of the $\ell=2-5$ multipoles and their dependence on frequency, sky cut and foreground correction. Since the construction of the filter takes into account correlations of the lower order modes with higher order modes, it significantly improves the accuracy of multipole estimation in comparison with the direct inversion method used by Efstathiou (2003a).

Our studies of the dependence on frequency of the multipole amplitudes showed that:

- the Kp2 mask is insufficient to remove strong foreground contamination near the Galactic plane for the K and Ka frequency bands even for the foreground corrected WMAP data,
- small deviations between the $\ell=3,4,5$ multipole determined from the Q, V and W frequency bands indicates that, after foreground cleaning, these multipoles are dominated by the CMB anisotropy component outside the Kp2 mask,
- the octopole preferred axis, approximately $(l,b) \sim (308^{\circ}, 63^{\circ})$, shows deviations of order two degrees for the Q, V and W frequency bands,
- noticeable changes of the quadrupole suggest a non-negligible residual foreground emission.

That the quadrupole (and to a lesser extent $\ell=4$) may be compromised by such residuals is supported by the changes observed after the application of increasing sky cuts. It also appears that the estimation of the quadrupole is sensitive to the dust absorption correction of the free-free template and free-free haze correction. This may provide yet further independent confirmation of significant contamination of the quadrupole by residual Galactic foregrounds.

Further tests of the sensitivity of the multipoles to the spectral dependence of the foreground emission have utilised a linear projection technique for foreground removal. Studies of the dependence of the multipole amplitudes and morphologies on the dust and synchrotron spectral indices showed that:

- multipoles $\ell=3,4,5$ are independent of the indices and do not vary with respect to them,
- increase of the synchrotron spectral index shifts hotter spots toward the Galactic poles and enhances amplitude of the quadrupole,
- increase of the dust spectral index shifts hotter spots toward the Galactic plane and decreases amplitude of the quadrupole.

In conclusion, it remains premature to make definitive statements in relation to the quadrupole. Large uncertainties of the quadrupole preferred axis should substantially increase the very low probabilities of the WMAP quadrupole-octopole alignment estimated by de Oliveira-Costa et al. (2003) and other quadrupole correlations studied by Schwarz et al. (2004). To similar conclusion came also Slosar & Seljak (2004) who showed that much of the alignment between quadrupole and octopole is due to foreground contamination. Nevertheless, estimates of $\ell=3,4,5$ are quite robust, and consistent with previous values. The observed

anisotropy structures are also present for in *COBE*-DMR data, and are therefore unlikely to be associated with instrumental systematic artifacts.

13 ACKNOWLEDGMENTS

We acknowledge the use of CMBFAST (Seljak & Zaldarriaga 1996). Some of the results in this paper have been derived using the HEALPix (Górski et al. 1998) software and analysis package. We acknowledge the use of the Legacy Archive for Microwave Background Data Analysis (LAMBDA). Support for LAMBDA is provided by the NASA Office of Space Science. PB acknowledges the financial support provided through the European Community's Human Potential Programme under contract HPRN-CT-2000-00124, (CMBNET), and Max-Planck-Institut fuer Astrophysik in Garching where parts of this work were carried out.

REFERENCES

Banday A.J., Dickinson C., Davies R.D., et al. 2003, astro-ph/0302181

Bennett C.L., Smoot G.F., Hinshaw G., et al. 1992, ApJ, 396, L7 Bennett C.L., Banday A.J., Górski K.M., et al. 1996, ApJ, 464, 1.1

Bennett C.L., Halpern M., Hinshaw G., et al. 2003a, preprint (astro-ph/0302207)

Bennett C.L., Hill R.S., Hinshaw G., et al. 2003b, preprint (astro-ph/0302208)

Bond J.R., Efstathiou G. 1987, MNRAS, 226, 655

Copi C.J., Huterer D., Starkman G.D., 2003, preprint (astro-ph/0310511)

Cornish N.J., Spergel D.N., Starkman G.D., Komatsu E., 2003, preprint (astro-ph/0310233)

Dickinson C., Davies R.D., Davis R.J., 2003, MNRAS, 341,369 Draine B.T., Lazarian A., 1998, ApJ, 494, L19

Dupac X., Giard M., Bernard J.-P., et al. 2002, A&A, 392, 691

Efstathiou G., 2003a, preprint (astro-ph/0306431)

Efstathiou G., 2003b, preprint (astro-ph/0310207)

Eriksen H.K., Banday A.J., Górski K.M., et al. 2004a, preprint (astro-ph/0403098)

Eriksen H.K., Hansen F.K., Banday A.J., et al. 2004b, ApJ, 605, 14

Fabbri R., Lucchin F., Matarrese S., 1987, ApJ, 315, 1

Finkbeiner D.P., 2003a, ApJS, 146, 407

Finkbeiner D.P., 2003b, preprint (astro-ph/0311547)

Finkbeiner D.P., Davis M., Schlegel D.J., 1999, ApJ, 524, 867

Gould A., 1993, ApJ, 403, L51

Górski K.M., 1994, ApJ, 430, L85

Górski, K.M., 1997, in Bouchet, F.R. et al., eds, Proceedings of the XVIth Moriond Astrophysics Meeting, Microwave Background Anisotropies, Editions Frontieres, p. 77

Górski K.M., Banday A.J., Bennett C.L., et al. 1996, ApJ, 464, L11

Górski K.M., Hivon E., Wandelt B.D., 1998, in Banday A.J., Seth R., Da Costa L., eds, Proceedings of the MPA/ESO Cosmology Conference, Evolution of Large Scale Structure

Haslam C.G.T., Klein U., Salter C.J., et al. 1981, A&A, 100, 209
 Hinshaw G, Spergel D.N., Verde L., et al. 2003, preprint (astro-ph/0302217)

Hobson M.P., Jones A.W., Lasenby A.N., et al. 1998, MNRAS, 300, 1

Kogut A., Banday A.J., Bennett C.L., et al. 1996, ApJ, 464, L5 Larson D.L., Wandelt B.D., 2004, preprint (astro-ph/0404037) Luminet J-P., Weeks J., Riazuelo A., et al. 2003, Nat, 425, 593 Maartens R., Ellis G.F.R., Stoeger W.R., 1996, A&A, 309, L7 de Oliveira-Costa A., Tegmark M., Zaldarriaga M., et al. 2003, preprint (astro-ph/0307282)

Seljak U., Zaldarriaga M., 1996, ApJ, 469, 437

Slosar A., Seljak U., 2004, preprint (astro-ph/0404567)

Smoot G.F., Bennett C.L., Kogut A., et al. 1992, ApJ, 396, L1 Stark Ph.B., 1993, ApJ, 408, L73

Schwarz D.J., Starkman G.D., Huterer D., et al. 2004, preprint (astro-ph/0403353)

Tegmark M., de Oliveira-Costa A., Hamilton A.J., 2003, preprint (astro-ph/0302496)

Vielva P., Martínez-González E., Barreiro R.B., et al. 2003, preprint (astro-ph/0310273)

APPENDIX A: THE CUT-SKY DECOMPOSITION

The spherical harmonics functions⁷, $Y_{\ell m}$, are commonly used as a decomposition basis on the sphere. However, utilising anything less than full sky coverage in the available data results in the loss of their orthogonality. One approach to circumvent this is to determine a set of orthonormal functions on an incomplete sphere. A practical implementation of the Gram-Schmidt orthogonalization of a set of linearly independent vectors was proposed by Górski (1994). Then, analysis of the cut-sky maps is performed in $(\ell_{\text{max}} + 1)^2$ -dimensional linear space spanned by the orthonormal functions ψ , which are linear combinations of the spherical harmonics with $\ell \leq \ell_{\text{max}}$. Now we will briefly present the required formalism and basic relations (more details can be found in the original paper, Górski 1994):

- bold letters denote matrices (upper case) and vectors (lower case).
- an index pair (ℓ, m) is mapped into a single index $i = \ell^2 + \ell + m + 1$, the inverse mapping in given by $\ell = \text{integer}(\sqrt{i-1})$ and $m = i (\ell^2 + \ell + 1)$,
- brackets $\langle \rangle$ denote an average over the ensemble and brackets $\langle \rangle_{\{\text{cut sky}\}}$ the scalar product specified to the pixelized cut sky, $\langle fg \rangle_{\{\text{cut sky}\}} \equiv \Omega_{\text{pix}} \sum_{p \in \{\text{cut sky}\}} f(p)g(p)$, where f and g are any functions on the sphere, p is a pixel label and Ω_{pix} is pixel solid angle,
- the coupling matrix, **W**, for the spherical harmonics on the cut sky is expressed by $\mathbf{W} \equiv \left\langle \tilde{\mathbf{y}} \cdot \tilde{\mathbf{y}}^T \right\rangle_{\text{[cut sky]}}$, where $\tilde{\mathbf{y}}$ is a $(\ell_{\text{max}} + 1)^2$ -dimensional vector of the spherical harmonics multiplied by the pixel window function, w_{ℓ}^{pix} ,
- the coupling matrix, W, is Choleski-decomposed into the product of a lower triangular matrix L and its transpose, $W = L \cdot L^T$,
- a new set of functions, $\psi(p) = \mathbf{L}^{-1} \cdot \tilde{\mathbf{y}}(p)$, is orthonormal on the pixelized cut sky,

$$Y_{\ell m}(\theta,\phi) = \sqrt{\frac{2\ell+1}{2}} \sqrt{\frac{(\ell-|m|)!}{(\ell+|m|)!}} P_{\ell}^{|m|}(\cos\theta) f(\phi) ,$$

where $f(\phi) = \left((2\pi)^{-1/2}, \ \pi^{-1/2}\cos m\phi \text{ or } \pi^{-1/2}\sin |m|\phi\right)$, for m=0,>0, or <0. $P_{\ell}^m(x)=^{m>0}(-1)^m(1-x^2)^{m/2}\frac{d^m}{dx^m}P_{\ell}(x)$, where $P_{\ell}(x)=\frac{1}{2^{\ell}\ell!}\frac{d^{\ell}}{dx^{\ell}}(x^2-1)^{\ell}$ are Legendre polynomials.

- the vector of decomposition coefficients, \mathbf{c} , of the CMB anisotropy map, ΔT , in ψ -base, $\mathbf{c} = \langle \Delta T(p)\psi(p) \rangle_{\text{[cut sky]}}$, is related to the vector of decomposition coefficients in the spherical harmonics basis, \mathbf{a} , by $\mathbf{c} = \mathbf{L}^T \cdot \mathbf{a}$,
- subscripts \mathcal{L} and \mathcal{H} denote a range of indices $i=1,\ldots,(\ell_{\rm rec}+1)^2$ and $i=(\ell_{\rm rec}+1)^2+1,\ldots,(\ell_{\rm max}+1)^2$, respectively, where $\ell_{\rm rec}$ is the highest order of the restored multipoles and $\ell_{\rm max}$ is the highest order of multipole which is taken into account in the analysis,
- all relevant quantities are multiplied by the appropriate pixel, $w_{\ell}^{\rm pix}$, or beam, $w_{\ell}^{\rm beam}$, window functions.

APPENDIX B: WIENER FILTER AND BAYES' THEOREM

Bayes' theorem states that, given a hypothesis H and some data D the posterior probability Pr(H|D) is the product of the likelihood Pr(D|H) and the prior probability Pr(H), normalized by the evidence Pr(D)

$$Pr(H|D) = \frac{Pr(H)Pr(D|H)}{Pr(D)}.$$

In our case the data consist of the $(\ell_{rec} + 1)^2$ numbers in the data vector \mathbf{c} , and we take the 'hypothesis' to consist of the $(\ell_{rec} + 1)^2$ numbers in the vector $\mathbf{a}_{\mathcal{L}}$. We then choose as our estimator, $\hat{\mathbf{a}}_{\mathcal{L}}$, vector which maximizes the posterior probability $\Pr(\mathbf{a}_{\mathcal{L}}|\mathbf{c})$. We must therefore maximize with respect to $\mathbf{a}_{\mathcal{L}}$ the quantity

$$Pr(\mathbf{a}_{\mathcal{L}}|\mathbf{c}) \propto Pr(\mathbf{c}|\mathbf{a}_{\mathcal{L}})Pr(\mathbf{a}_{\mathcal{L}})$$
,

which is the product of the likelihood $\Pr(\mathbf{c}|\mathbf{a}_{\mathcal{L}})$ and the prior $\Pr(\mathbf{a}_{\mathcal{L}})$. If we took the prior probability to be uniform in the components of vector $\mathbf{a}_{\mathcal{L}}$, it would be equivalent to maximizing the likelihood function $\Pr(\mathbf{c}|\mathbf{a}_{\mathcal{L}})$. However, we will take the prior probability to be a multivariate Gaussian of the form $\Pr(\mathbf{a}_{\mathcal{L}}) \propto \exp\left(-\mathbf{a}_{\mathcal{L}}^T \cdot \mathbf{S}_{\mathcal{L}\mathcal{L}}^{-1} \cdot \mathbf{a}_{\mathcal{L}}/2\right)$, where $\mathbf{S}_{\mathcal{L}\mathcal{L}} = \left\langle \mathbf{a}_{\mathcal{L}} \cdot \mathbf{a}_{\mathcal{L}}^T \right\rangle$. This form of the prior is confirmed very well by observations.

If we assume that the data vector is the sum $\mathbf{c} = \mathbf{L}_{\mathcal{L}\mathcal{L}}^T \cdot \mathbf{a}_{\mathcal{L}} + \mathbf{L}_{\mathcal{H}\mathcal{L}}^T \cdot \mathbf{a}_{\mathcal{H}} + \mathbf{n}_{\psi}$ and $\mathbf{a}_{\mathcal{H}}$ and \mathbf{n}_{ψ} are Gaussian, then the likelihood function will also be a multivariate Gaussian of the form

$$\Pr(\mathbf{c}|\mathbf{a}_{\mathcal{L}}) \propto \exp\left[-(\mathbf{c} - \mathbf{L}_{\mathcal{L}\mathcal{L}}^{T} \cdot \mathbf{a}_{\mathcal{L}})^{T} \cdot \mathbf{C}_{\psi}^{-1} \cdot (\mathbf{c} - \mathbf{L}_{\mathcal{L}\mathcal{L}}^{T} \cdot \mathbf{a}_{\mathcal{L}})/2\right] / \sqrt{\det \mathbf{C}_{\psi}}, (B1)$$

where the covariance matrix $\mathbf{C}_{\psi} = \mathbf{L}_{\mathcal{HL}}^T \cdot \mathbf{S}_{\mathcal{HH}} \cdot \mathbf{L}_{\mathcal{HL}} + \mathbf{N}_{\psi}$ and the noise covariance matrix in ψ -base is given by

$$\mathbf{N}_{\psi} = \left\langle \mathbf{n}_{\psi} \cdot \mathbf{n}_{\psi}^{T} \right\rangle = \Omega_{\text{pix}} \left\langle \sigma^{2}(p)_{\text{noise}} \ \psi(p) \cdot \psi^{T}(p) \right\rangle_{p \in \{\text{cut sky}\}} \ . \tag{B2}$$

One should notice that the expression in square brackets in (B1) is simply the χ^2 expression. Therefore, the posterior probability takes the form

$$\Pr(\mathbf{a}_{\mathcal{L}}|\mathbf{c}) \propto \exp\left(-\chi^2(\mathbf{a}_{\mathcal{L}})/2 - \mathbf{a}_{\mathcal{L}}^T \cdot \mathbf{S}_{\mathcal{L}}^{-1} \cdot \mathbf{a}_{\mathcal{L}}/2\right). \tag{B3}$$

Since, for a given set of observations, the data vector \mathbf{c} and the covariance matrices are fixed, the problem of maximizing the posterior probability with respect to $\mathbf{a}_{\mathcal{L}}$ is equivalent to minimizing the function

$$\Phi(\mathbf{a}_{\mathcal{L}}) = \chi^2(\mathbf{a}_{\mathcal{L}}) + \mathbf{a}_{\mathcal{L}}^T \cdot \mathbf{S}_{\mathcal{L}\mathcal{L}}^{-1} \cdot \mathbf{a}_{\mathcal{L}}. \tag{B4}$$

Then the estimate $\hat{\mathbf{a}}_{f}$ of the vector \mathbf{a}_{f} is given by

$$\hat{\mathbf{a}}_{\mathcal{L}} = \left(\mathbf{L}_{\mathcal{L}\mathcal{L}} \cdot \mathbf{C}_{\psi}^{-1} \cdot \mathbf{L}_{\mathcal{L}\mathcal{L}}^{T} + \mathbf{S}_{\mathcal{L}\mathcal{L}}^{-1} \right)^{-1} \cdot \mathbf{L}_{\mathcal{L}\mathcal{L}} \cdot \mathbf{C}_{\psi}^{-1} \cdot \mathbf{c}_{\mathcal{L}} \equiv \mathbf{F} \cdot \mathbf{c}_{\mathcal{L}} . \tag{B5}$$

It can be shown that the matrix \mathbf{F} is identical to the Wiener filter matrix (10). Thus, we find that by assuming a Gaussian prior in Bayes' theorem, we recover the standard Wiener filter.

⁷ we use real valued functions:

APPENDIX C: COVARIANCE MATRIX

The posterior probability is a multivariate Gaussian of the form

$$\text{Pr}(\boldsymbol{a}_{\mathcal{L}}|\boldsymbol{c}) \propto \text{exp}\left(-(\boldsymbol{a}_{\mathcal{L}} - \boldsymbol{\hat{a}}_{\mathcal{L}})^T \cdot \boldsymbol{M}^{-1} \cdot (\boldsymbol{a}_{\mathcal{L}} - \boldsymbol{\hat{a}}_{\mathcal{L}})/2\right) / \sqrt{\det \boldsymbol{M}} \;, \quad (C1)$$

which has its maximum value at the estimate $\hat{\mathbf{a}}_{\mathcal{L}}$ of the signal vector and \mathbf{M} is the covariance matrix defined by $\mathbf{M} \equiv \left\langle (\mathbf{a}_{\mathcal{L}} - \hat{\mathbf{a}}_{\mathcal{L}}) (\mathbf{a}_{\mathcal{L}} - \hat{\mathbf{a}}_{\mathcal{L}})^T \right\rangle$. The diagonal terms of the covariance matrix \mathbf{M} are the squared errors $\Delta \mathbf{a}_{\mathcal{L}}$ of the estimate $\hat{\mathbf{a}}_{\mathcal{L}}$ and non-diagonal elements of the matrix represent correlations between errors. However, to study correlations a more convenient representation of the correlation matrix is used – the covariance matrix normalized by its diagonal terms, $\mathbf{M}_{ij} / \sqrt{\mathbf{M}_{ii} \mathbf{M}_{jj}}$ ($i, j \in [5, \dots, (\ell_{\text{rec}} + 1)^2]$). Then, the coefficient of correlation between uncertainty in \mathbf{a}_i and uncertainty in \mathbf{a}_j is a number between -1 and 1.

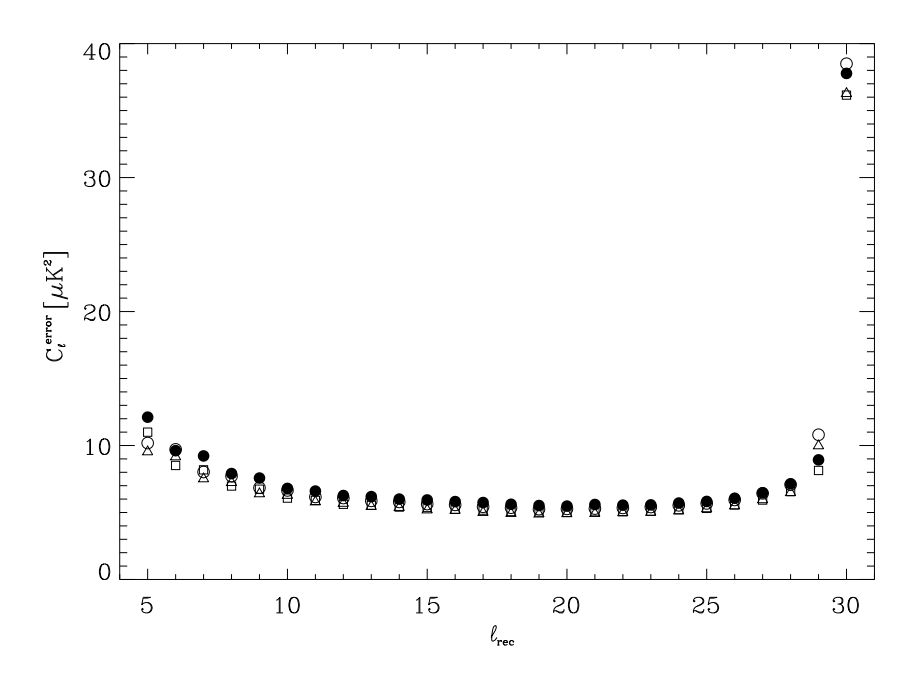


Figure 1. The rms of the difference between the input and output multipole maps as a function of ℓ_{rec} . Filled circle, empty circle, square and triangle denote C_ℓ^{error} for multipoles $\ell=2,3,4,5$, respectively.

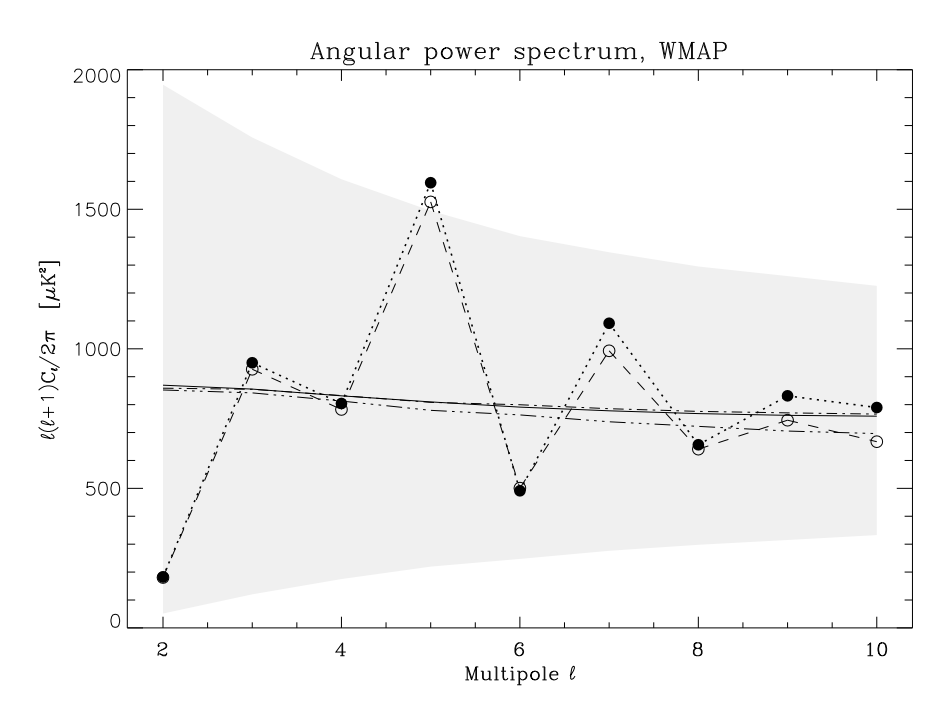


Figure 2. Comparison of the power spectra of the WMAP map, masked by the Kp2 mask, restored by the Wiener (open circles) and PE (filled circles) filters. Dash dot dot and dash dot lines correspond to the averaged power spectra derived from the Wiener and PE filter reconstruction of 10^4 simulated WMAP maps respectively. The smooth curve shows the WMAP team best fit ΛCDM model ($\Omega_{\Lambda}=0.73$ and $\Omega_{m}=0.27$) with running spectral index. The grey band indicates the cosmic variance errors (95% confidence level).

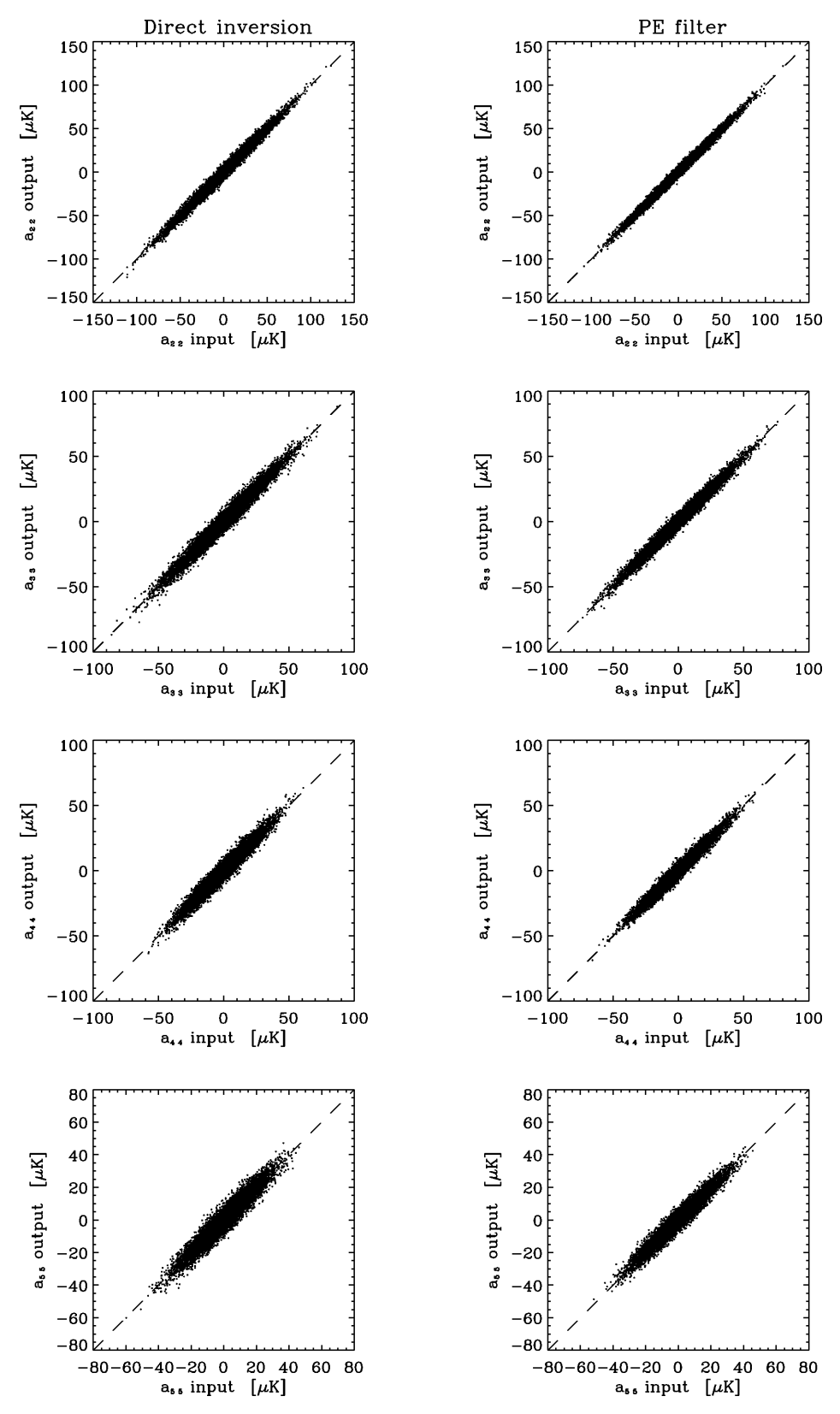


Figure 3. Comparison of the accuracy of estimation of the $a_{\ell,\ell}$ modes using the direct inversion and PE filtering reconstruction methods, determined from simulations with the Kp2 mask. The abscissae give the input values of harmonic coefficients used to generate the simulated skies. The ordinates give the output values from the direct inversion (left column) and PE filtering (right column) methods. The coupling matrix was truncated at $\ell_{rec} = 10$ in the direct inversion method.

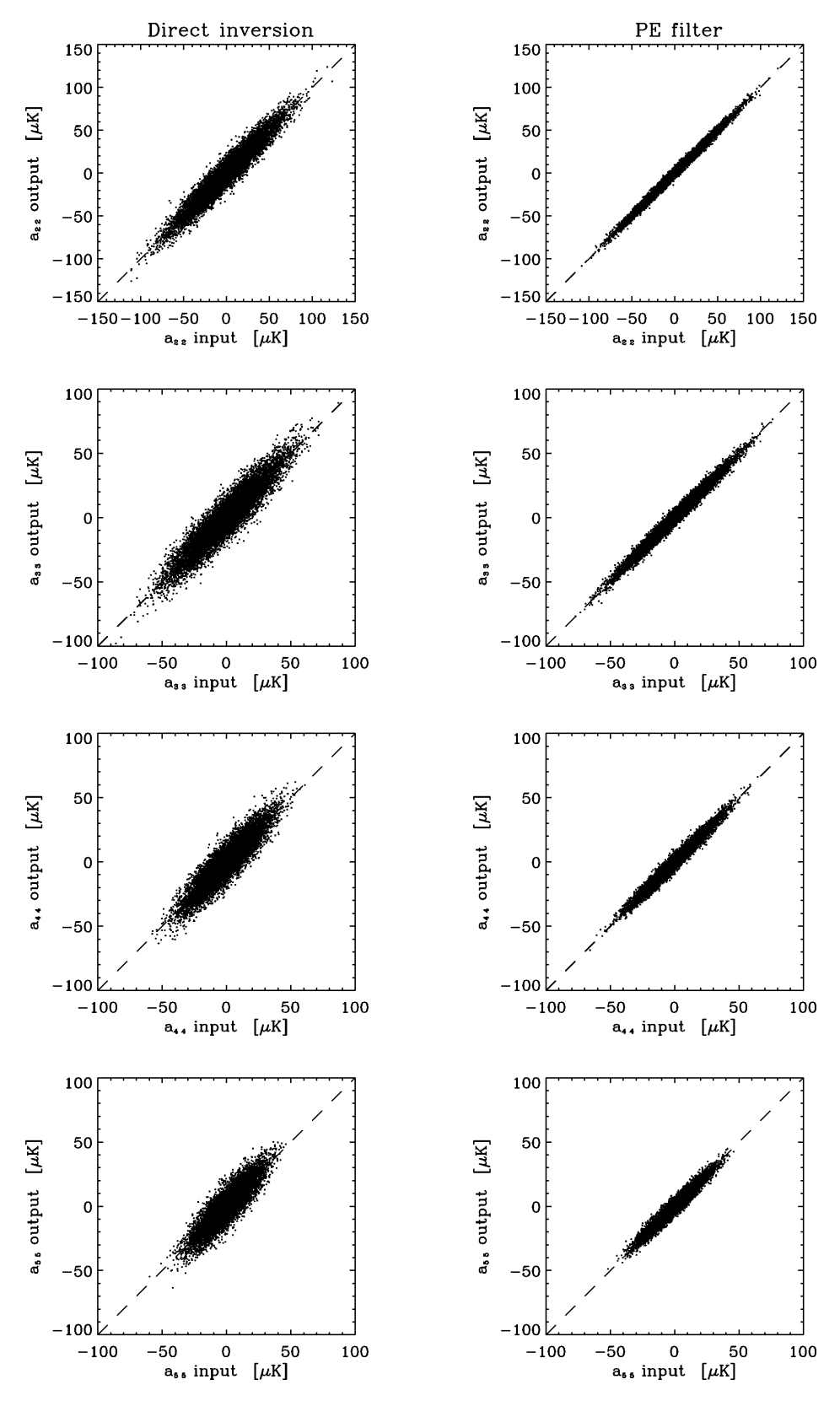


Figure 4. The same as Fig. (3) but with the coupling matrix truncated at $\ell_{rec} = 30$ in the direct inversion method.

Figure 5. Maps of the WMAP $\ell = 2, ..., 5$ multipoles, computed by the PE filtering of the WMAP corrected coadded map (first row), TOH cleaned map (second row) and ILC map (third row) after applying the Kp2 mask.

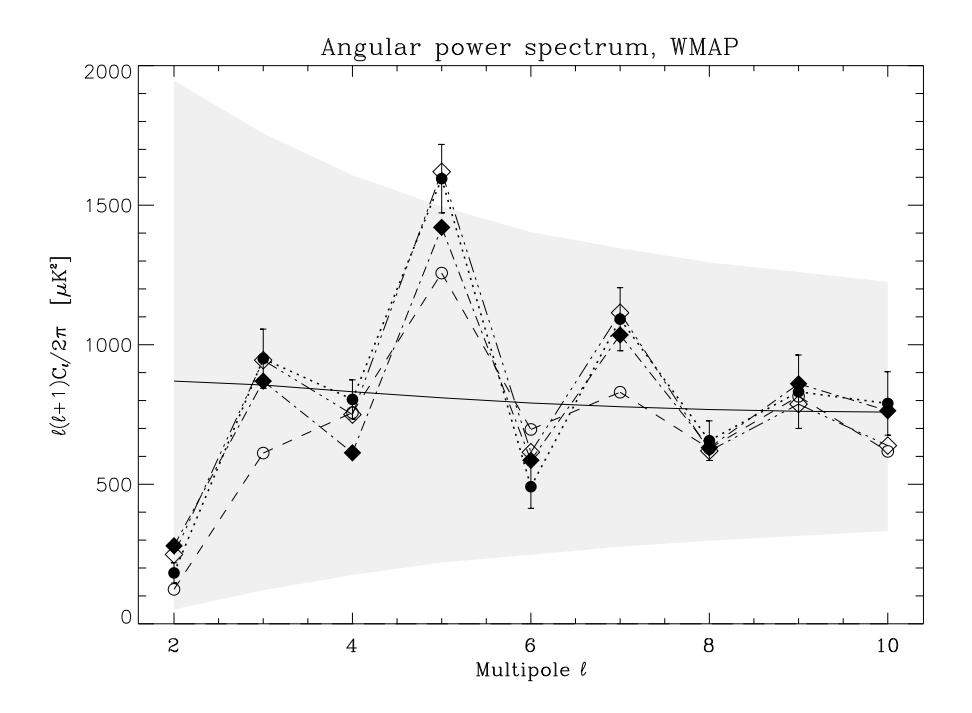


Figure 6. Angular power spectrum of the WMAP data. The power spectrum from the Hinshaw et al. cut sky WMAP analysis (open circles) is compared with those obtained by the PE filtering of the TOH (filled diamonds), ILC (open diamonds) and corrected coadded map (filled circles), masked by the Kp2 mask. The error bars (68% confidence level) of our WMAP power spectrum estimates are shown. They do not take into account cosmic variance. The major contribution to the errors comes from the correlations between the restored multipoles and between the restored and higher multipoles. The noise contribution is negligible. The smooth curve shows the WMAP team best fit ΛCDM model ($\Omega_{\Lambda} = 0.73$ and $\Omega_{m} = 0.27$) with running spectral index. The grey band indicates the cosmic variance errors (95% confidence level).

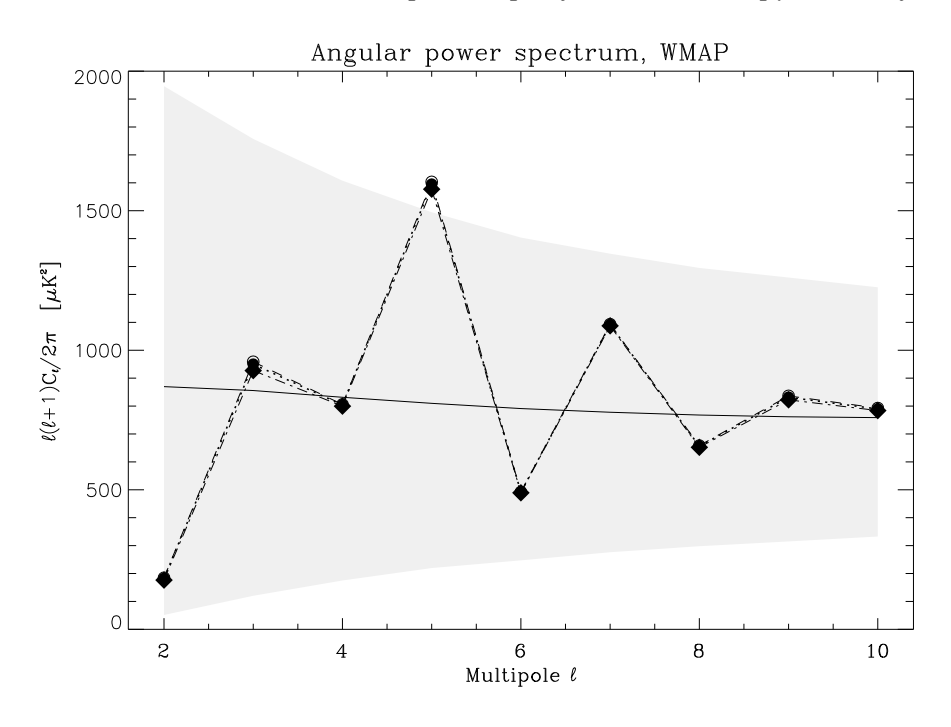


Figure 7. Sensitivity of the derived WMAP angular power spectrum to the input power spectrum used in the construction of the PE filter. Filled circles correspond to the spectrum of the multipoles obtained assuming the best fit to the WMAP data ΛCDM model power spectrum (indicated by the solid line). The open circles and filled diamonds correspond, respectively, to the same assumed power spectrum but after adding and subtracting the square root of the cosmic variance (indicated by the shaded band, 95% confidence level).

Figure 8. Maps of the $\ell = 2, ..., 5$ WMAP multipoles determined from the different frequency bands.

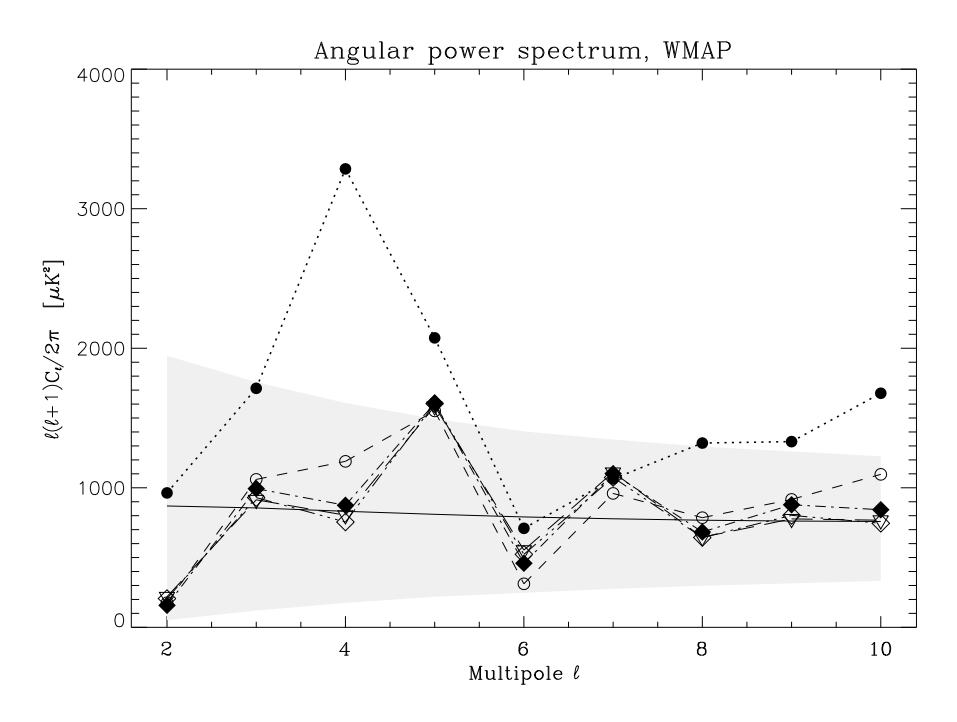


Figure 9. The angular power spectrum of the WMAP data for K-band (filled circles), Ka-band (open circles), Q-Band (filled diamonds), V-Band (open diamonds) and W-Band (triangle) maps obtained by PE filtering for the Kp2 mask. The smooth curve shows the WMAP team best fit ΛCDM model ($\Omega_{\Lambda}=0.73$ and $\Omega_{m}=0.27$) with running spectral index. The grey band indicates the cosmic variance errors (95% confidence level).

Figure 10. Maps of the $\ell = 2, ..., 5$ *WMAP* multipoles for different masks: Kp2, Kp0, '20+' and '30'.

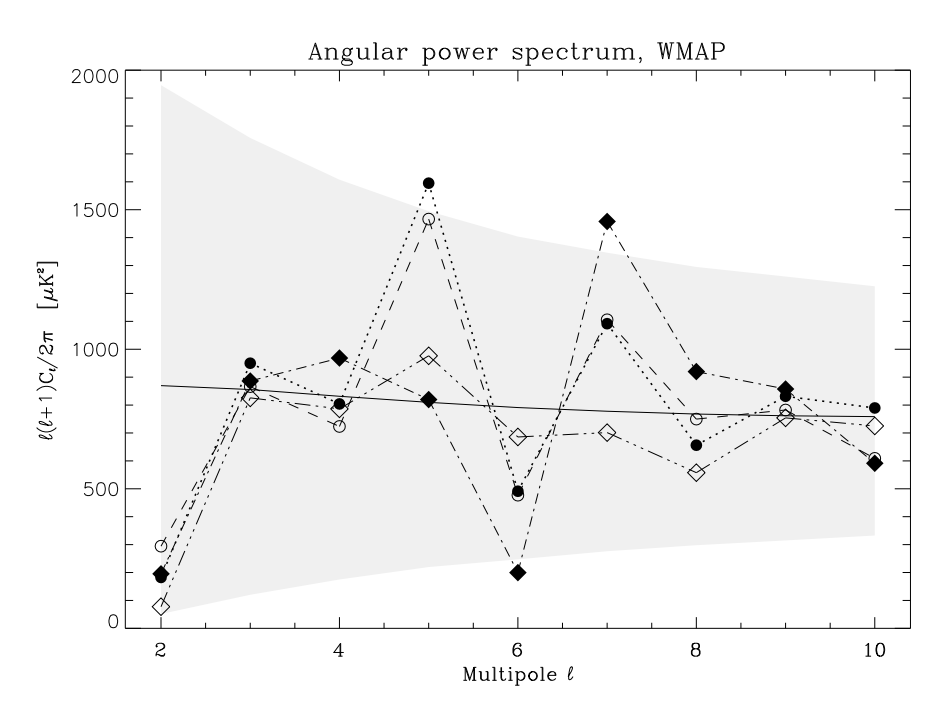


Figure 11. The angular power spectra of the WMAP data obtained by the PE filtering of the corrected coadded Q+V+W map after masking with the Kp2 (filled circles), Kp0 (open circles), '20+' (filled diamonds) and '30' (open diamonds) masks. The smooth curve shows the WMAP team best fit ΛCDM model ($\Omega_{\Lambda} = 0.73$ and $\Omega_{m} = 0.27$) with running spectral index. The grey band indicates the cosmic variance errors (95% confidence level).

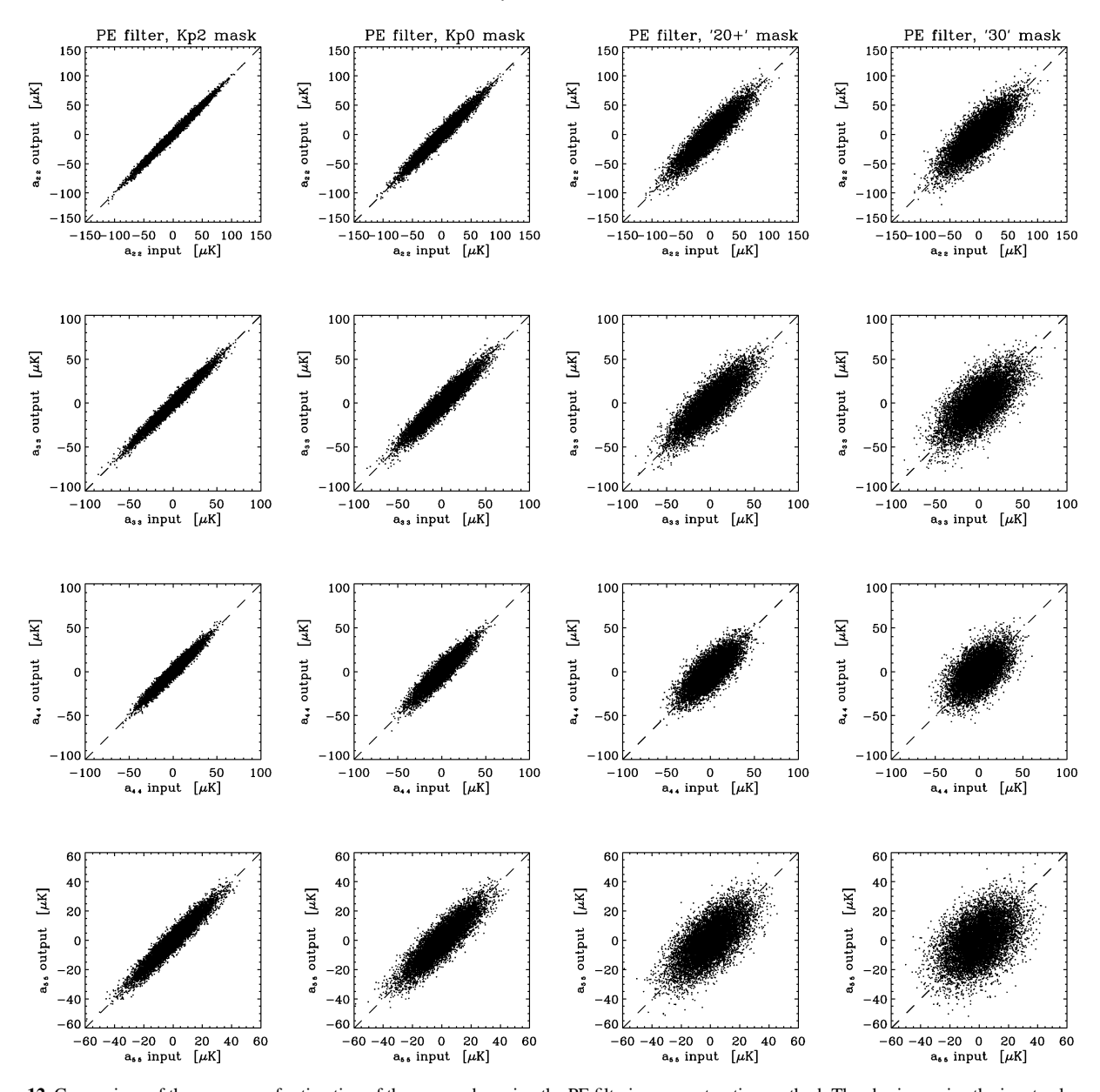


Figure 12. Comparison of the accuracy of estimation of the $a_{\ell,\ell}$ modes using the PE filtering reconstruction method. The abscissae give the input values of the harmonic coefficients used to generate the simulated skies. The ordinates give the output values determined after application of the Kp2 mask (first column), Kp0 mask (second column), '20+' mask (third column) and '30' mask (fourth column).

Figure 13. The Δ_{error}^2 maps (see text) corresponding to the sum of the errors for the restored $\ell = 2, ..., 5$ WMAP multipoles (centre) and for each multipole separately. The maps are shown in logarithmic scale.

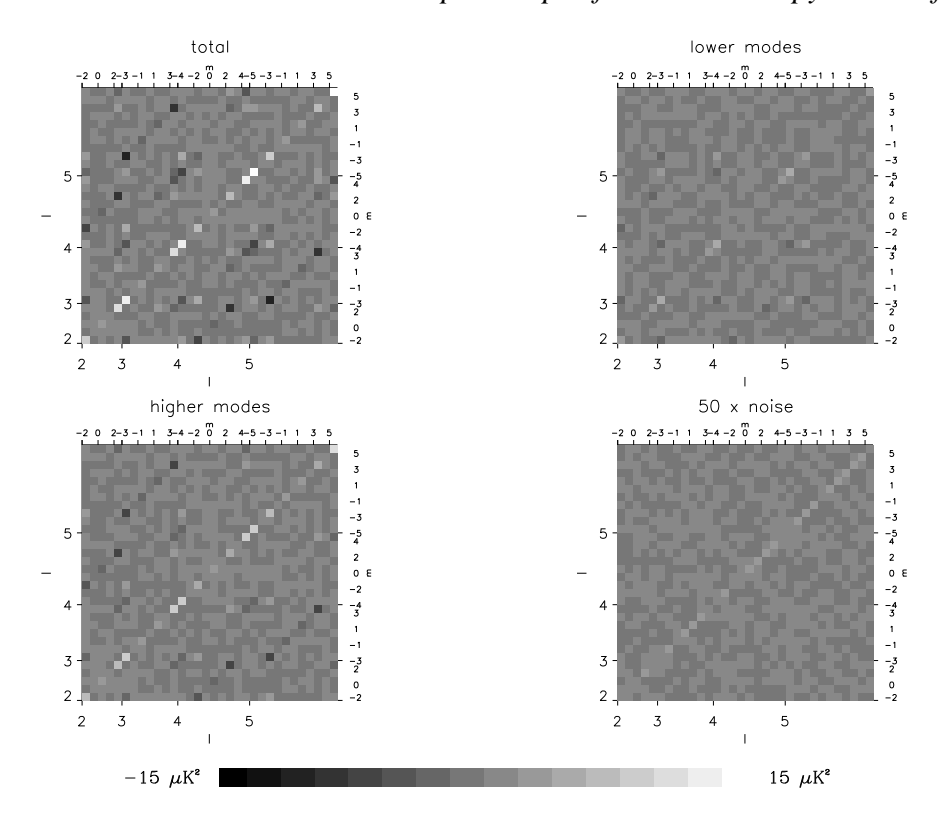


Figure 14. Decomposition of the covariance matrix for the PE filtering of the WMAP data into specific contributions is shown. The total covariance matrix (upper left figure) is compared with the components induced by: correlations between restored multipoles (upper right figure), correlations of restored multipoles with higher order multipoles (bottom left figure) and noise correlations (bottom right figure). Only that part of the matrices corresponding to the range $\ell = 2, ..., 5$ are shown. The noise component is multiplied by 50 to render it visible. Maximal correlation is at most $\sim 14 \,\mu\text{K}^2$ and minimal down to $\sim -11 \,\mu\text{K}^2$. The modes are ordered such that index i is given by $i = \ell^2 + \ell + m + 1$.

Figure 15. The multipoles map obtained by the PE filtering of the CMB maps after masking by the Kp2 mask. The CMB maps were derived from the *WMAP* data as corrected by four variants for the free-free emission. From top to bottom, the maps for following variants of the correction are shown: for Hα template uncorrected for dust absorption and no free-free haze correction, for Hα template corrected for dust absorption and free-free haze correction, for Hα template corrected for dust absorption and free-free haze correction. Spectral indices of the thermal dust and synchrotron emission were $β_d = 2.2$ and $β_s = -3.1$, respectively.

Figure 16. The $\ell = 2$ quadrupole component obtained by PE filtering of the CMB maps after masking by the Kp2 mask. The CMB maps were derived from the *WMAP* maps corrected for the free-free emission (with H α template corrected for dust absorption and free-free haze template) for various spectral indices of the dust β_{dust} and synchrotron β_{sych} indices.

Figure 17. Maps of the $\ell = 2, ..., 5$ multipoles recovered using the PE filter for *COBE*-DMR (the first column) and *WMAP* data (the second column). In both cases the extended Galactic cut was used.

